

# Quasiparticle self-consistent $GW$ method: methodological details

Takao Kotani and Mark van Schilfgaarde  
*School of Materials, Arizona State University, Tempe, AZ, 85284*

Sergey V. Faleev  
*Sandia National Laboratories, Livermore, CA 94551*  
(Dated: January 25, 2020)

We have developed a new type of self-consistent scheme within the  $GW$  approximation, which we call quasiparticle self-consistent  $GW$  (QSGW). We have shown that QSGW rather well describes energy bands for a wide-range of materials, including many where the local-density approximation fails. QSGW contains physical effects found in other theories such as LDA+ $U$ , SIC and  $GW$  in a satisfactory manner without many of their drawbacks (partitioning of itinerant and localized electrons, adjustable parameters, ambiguities in double-counting, etc.) We present some theoretical discussion concerning the formulation of QSGW, including a prescription for calculating the total energy. We also address several key methodological points needed for implementation. We then show convergence checks and some representative results in a variety of materials.

PACS numbers: 71.15.-m,71.10.-w,71.20.-b

In 1986, Hybertsen and Louie [1] first implemented Hedin's  $GW$  approximation ( $GWA$ ) [2] within an *ab-initio* framework. It is a perturbation treatment starting from the Kohn-Sham eigenfunctions and eigenvalues given in the local density approximation (LDA) to density functional theory (DFT)[3, 4]. We will denote this approach here as 1shot- $GW$ . Until now 1shot- $GW$  has been applied to variety of materials, usually in conjunction with the pseudopotential (PP) approximation. Quasiparticle (QP) energies so obtained are in significantly better agreement with experiments than the LDA Kohn-Sham energies[5].

However, we have recently shown that 1shot- $GW$  has many significant failings. Even in simple semiconductors it systematically underestimates optical gaps[6, 7, 8, 9]. In general, the quality of results are closely tied to the quality of the LDA starting point. For more complicated cases where the LDA eigenfunctions are poor, 1shot- $GW$  can fail even qualitatively[9]. To overcome this difficulty, we have developed a new *ab-initio* approach to  $GW$  [10, 11, 12, 13], which we now call "quasiparticle self-consistent  $GW$ " (QSGW) method. QSGW is a first-principles method that stays within the framework of Hedin's  $GWA$ , that is, QSGW is a perturbation theory built around some noninteracting Hamiltonian. It does not depend on the LDA but rather determines the optimum noninteracting Hamiltonian in a self-consistent manner. We have shown that QSGW satisfactorily describes QP energies for a wide range of materials.

The present paper begins with a derivation the fundamental equation of QSGW, and some theoretical discussion concerning it (Sec. I). The fundamental equation is derived from the idea of a self-consistent perturbation. We also present a means for computing the total energy through the adiabatic connection formalism. Next, we detail a number of key methodological points (Sec. II). The present implementation is unique in that it makes no pseudopotential or shape approximation to the poten-

tial, and it uses a mixed basis for the response function, Coulomb interaction, and self-energy, which enables us to properly treat core states. The  $GWA$  methodology is presented along with some additional points particular to self-consistency. In Sec. III, we show some convergence checks, using GaAs as a representative system. Then we show how QSGW works by comparing it to other kinds of  $GWA$  for compounds representative of different materials classes: semiconductors C, Si, SiC, GaAs, ZnS, and ZnSe; oxide semiconductors ZnO and Cu<sub>2</sub>O; transition metal monoxides MnO and NiO; transition metals Fe and Ni.

## I. THEORY

### A. $GWA$

Let us summarize the prescription of ( $GWA$ ) [1, 2] for later discussion. Here we omit spin index for simplicity. Generally speaking, we can construct the  $GWA$  potential from some given one-body Hamiltonian  $H^0$  written as

$$H^0 = \frac{-\nabla^2}{2m} + V^{\text{eff}}(\mathbf{r}, \mathbf{r}'). \quad (1)$$

The one-particle effective potential  $V^{\text{eff}}(\mathbf{r}, \mathbf{r}')$  can be non-local, though when generated by the usual DFT it is local, i.e.  $V^{\text{eff}}(\mathbf{r}, \mathbf{r}') = V^{\text{eff}}(\mathbf{r})\delta(\mathbf{r} - \mathbf{r}')$ .  $H^0$  determines the set of eigenvalues  $\{\varepsilon_i\}$  and eigenfunctions  $\{\Psi_i(\mathbf{r})\}$ . From them we can construct the non-interacting Green function  $G^0$  as

$$G^0(\mathbf{r}, \mathbf{r}', \omega) = \sum_i \frac{\Psi_i(\mathbf{r})\Psi_i^*(\mathbf{r}')}{\omega - \varepsilon_i \pm i\delta}, \quad (2)$$

where  $-i\delta$  is for occupied states, and  $+i\delta$  for unoccupied states. Within the RPA (random-phase approximation),

the screened Coulomb interaction is

$$W = \epsilon^{-1}v = (1 - v\Pi)^{-1}v \quad (3)$$

where  $\Pi = -iG^0 \times G^0$  is the proper polarization function, and  $v(\mathbf{r}, \mathbf{r}') = \frac{e^2}{|\mathbf{r} - \mathbf{r}'|}$  is the bare Coulomb interaction.  $\epsilon$  denotes the dielectric function. As seen in works by Alouani and co-workers [14, 15],  $W$  calculated from a reasonable  $H^0$  should be in good agreement with experiments, even when  $W$  does not satisfy the  $f$ -sum rule when  $H^0$  is non-local [14] (because of the so-called scissors operator).

Hedin's  $GWA$  gives the self-energy  $\Sigma(\mathbf{r}, \mathbf{r}', \omega)$  as

$$\Sigma(\mathbf{r}, \mathbf{r}', \omega) = \frac{i}{2\pi} \int d\omega' G^0(\mathbf{r}, \mathbf{r}', \omega - \omega') W(\mathbf{r}, \mathbf{r}', \omega') e^{-i\delta\omega'}. \quad (4)$$

From this self-energy, the external potential  $V^{\text{ext}}$  from

the nuclei, and the Hartree potential  $V^{\text{H}}$  which is calculated from the electron density through  $G^0$ , we obtain an  $\omega$ -dependent one-body effective potential  $V^{GW}(\omega)$  :

$$V^{GW}(\omega) = V^{\text{ext}} + V^{\text{H}} + \Sigma(\omega). \quad (5)$$

For simplicity we omit arguments  $(\mathbf{r}, \mathbf{r}')$ .  $V^{\text{ext}}$  and  $V^{\text{H}}$  are local and  $\omega$ -independent potentials. Thus  $GWA$  gives the mapping  $V^{\text{eff}} \rightarrow V^{GW}(\omega)$ . In other words, the  $GWA$  generates a perturbative correction  $\Delta V(\omega)$  written as

$$\Delta V(\omega) = V^{GW}(\omega) - V^{\text{eff}} \quad (6)$$

to the one-particle potential  $V^{\text{eff}}$ .  $V^{GW}(\omega)$  and  $\Delta V(\omega)$  can be regarded as functionals of  $V^{\text{eff}}$  (or  $H^0$ ).

In the standard 1shot- $GW$  with  $H^0$  generated by the LDA,  $V^{\text{eff}}$  is the LDA Kohn-Sham Hamiltonian. Neglecting off-diagonal terms, the QP energy (QPE) is

---


$$E_{\mathbf{k}n} = \varepsilon_{\mathbf{k}n} + Z_{\mathbf{k}n} [\langle \Psi_{\mathbf{k}n} | \Sigma(\mathbf{r}, \mathbf{r}', \varepsilon_{\mathbf{k}n}) | \Psi_{\mathbf{k}n} \rangle - \langle \Psi_{\mathbf{k}n} | V_{\text{xc}}^{\text{LDA}}(\mathbf{r}) | \Psi_{\mathbf{k}n} \rangle], \quad (7)$$

where  $Z_{\mathbf{k}n}$  is the QP renormalization factor:

$$Z_{\mathbf{k}n} = \left[ 1 - \langle \Psi_{\mathbf{k}n} | \frac{\partial}{\partial \omega} \Sigma(\mathbf{r}, \mathbf{r}', \varepsilon_{\mathbf{k}n}) | \Psi_{\mathbf{k}n} \rangle \right]^{-1}. \quad (8)$$

Eq. (7) the customary way QPE's are calculated in  $GW$ . However, as we discussed in Ref. [9], using  $Z = 1$  instead of Eq. (8) is usually a better approximation; see also Sec.III. Chapter 7 of Ref.[16] presents another analysis in the context of the Frölich Hamiltonian, where  $Z = 1$  is shown to be a better approximation. In any case, we have to calculate matrix elements  $\langle \Psi_{\mathbf{k}n'} | \Sigma(\mathbf{r}, \mathbf{r}', \omega) | \Psi_{\mathbf{k}n} \rangle$  as accurately and as efficiently as possible (off-diagonal elements are necessary in the  $QSGW$  case, as explained below).

## B. Quasiparticle self-consistent $GW$

$QSGW$  is a formalism which determines  $V^{\text{eff}}$  self-consistently within the  $GWA$ . As we showed in Ref.[9], using the LDA to generate  $H^0$  is not necessarily a good approximation. For example, time-reversal symmetry is automatically enforced because  $V^{\text{eff}}$  is local (and thus real). This symmetry is strongly violated in open  $f$ -shell systems [13]. The bandgap of a relatively simple III-V semiconductor, InN, is close to zero[6, 7]; also the QP spectrum of NiO is little improved over LDA[10]. A variety of other examples could be cited where  $H^0 = H^{\text{LDA}}$  is a poor approximation.

One possible way to determine  $V^{\text{eff}}$  without DFT is based on the idea of self-consistency. If we can construct

a mapping  $V^{GW}(\omega) \rightarrow V^{\text{eff}}$ , we can close the equation to determine  $V^{\text{eff}}$ , i.e. determine  $V^{\text{eff}}$  self-consistently by  $V^{\text{eff}} \rightarrow V^{GW}(\omega) \rightarrow V^{\text{eff}} \rightarrow \dots$

In the following, we present a method to determine  $V^{GW}(\omega) \rightarrow V^{\text{eff}}$ , and derive the fundamental  $QSGW$  equation [10, 11, 12, 13]. We start from an assumption that

The optimum  $H^0$  for  $GWA$  exists, and is determined so as to minimize the perturbative correction  $\Delta V(\omega)$ , Eq. (6), generated by  $GWA$ .

We need a means to evaluate the size of  $\Delta V(\omega)$ . If  $\Sigma(\omega)$  were  $\omega$ -independent and hermitian, we could simply choose  $V^{\text{eff}}$  as  $V^{\text{eff}} = V^{\text{ext}} + V^{\text{H}} + \Sigma$ . Then  $\Delta V$  given by  $GWA$  is identically zero, i.e. as small as possible. Such  $V^{\text{eff}}$  should define the best perturbation theory because of the assumption. This is indeed the case in Hartree-Fock theory. However, we can not choose  $V^{\text{eff}}$  to be  $\Delta V(\omega) = 0$  because  $\Sigma(\omega)$  is  $\omega$ -dependent. Instead, we have to introduce some norm functional  $M[V^{\text{eff}}]$ , which defines the size of  $\Delta V(\omega)$  as a functional of  $V^{\text{eff}}$ . From a given norm  $M[V^{\text{eff}}]$ , we can determine  $V^{\text{eff}}$  that minimizes it.

Let us discuss how to choose the norm functional. The Green function  $G$  for  $H^0 + \Delta V(\omega)$  is determined by the equation of motion  $(\omega - H^0 - \Delta V(\omega)) G - \delta(\mathbf{r} - \mathbf{r}') = 0$ .

If  $\Delta V(\omega)$  is small enough, we can expect that  $G^0$  still almost satisfies the equation of motion;

$$(\omega - H^0 - \Delta V(\omega)) G^0 - \delta(\mathbf{r} - \mathbf{r}') \approx 0. \quad (9)$$

The left-hand side simplifies to  $\Delta V(\omega)G^0$ ; in any perturbation treatment based on  $G^0$ ,  $\Delta V(\omega)$  appears in this combination.  $\Delta V(\omega)G^0$  is expanded in  $\{\Psi_i\}$  as  $\Delta \bar{V}_{ij}(\omega) = \langle \Psi_j | \Delta V(\omega) | \Psi_i \rangle \frac{1}{\omega - \varepsilon_i \pm i\delta}$ . Generally speaking,  $\langle \Psi_j | \Delta V(\omega) | \Psi_i \rangle$  as function of  $\omega$  is smooth around  $E_{\text{Fermi}}$ , and contains plasmon-related parts at high energy (e.g., See Fig.17 in Ref.[2]). Thus the main structure of  $\Delta \bar{V}_{ij}(\omega)$  comes from the factor  $\frac{1}{\omega - \varepsilon_i \pm i\delta}$ , and the side structures come mainly from the plasmon-related parts. By the variation of  $V^{\text{eff}}$ , we can directly control the quantity  $\langle \Psi_j | \Delta V(\varepsilon_i) | \Psi_i \rangle$  which gives the amplitude of the main structure, though this variation will

much less affect the side structures. Thus, the quantity  $\langle \Psi_j | \Delta V(\varepsilon_i) | \Psi_i \rangle$  is used for the definition of the norm in order to optimize  $V^{\text{eff}}$  (note  $\omega$  is at  $\varepsilon_i$ ). Summing the squares of the quantity, we can define  $\bar{N}$  as the mean measure of smallness of the left-hand side of Eq. (9);  $\bar{N} = \sum_{i,j} |\langle \Psi_j | \Delta V(\varepsilon_i) | \Psi_i \rangle|^2$ . This can be rewritten as

$$\bar{N}[\Delta V(\omega), H^0] = \text{Tr} [\Delta V(\omega) \delta(\omega - H^0) \{\Delta V(\omega)\}^\dagger], \quad (10)$$

where the trace is taken over  $\omega$  and the vector space spanned by the basis sets defining  $H^0$ . Note  $\delta(\omega - H^0) = \sum_i |\Psi_i\rangle \delta(\omega - \varepsilon_i) \langle \Psi_i|$ , which is taken as the positive-definite weight in the usual inner product. Applying the same logic, we obtain  $\bar{N}[\{\Delta V(\omega)\}^\dagger, H^0]$  as a measure of the smallness of  $G^0(\omega - H^0 - \Delta V(\omega)) - \delta(\mathbf{r} - \mathbf{r}') \approx 0$ . As the average of this norm and Eq. (10) we define

$$N[\Delta V(\omega), H^0] = \frac{1}{2} \bar{N}[\Delta V(\omega), H^0] + \frac{1}{2} \bar{N}[\{\Delta V(\omega)\}^\dagger, H^0]. \quad (11)$$

This functional satisfies time-reversal symmetry.  $\Delta V(\omega)$  is a functional of  $V^{\text{eff}}$  because the  $GWA$  determines it from  $H^0$ , as we explained previously. We can write  $\Delta V$  as  $\Delta V(\omega, [V^{\text{eff}}])$  and define

$$M[V^{\text{eff}}] = N[\Delta V(\omega, [V^{\text{eff}}]), H^0], \quad (12)$$

as a functional of  $V^{\text{eff}}$  ( $H^0$  is a trivial functional of  $V^{\text{eff}}$ , see Eq. (1)).  $M$  is the same as Eq. (1) in Ref. [11].  $V^{\text{eff}}$  should be chosen by minimization of  $M[V^{\text{eff}}]$ . This will minimize the size of  $\Delta V(\omega)$  under the restriction that  $V^{\text{eff}}$  is hermitian.

We now solve the minimization problem of  $M[V^{\text{eff}}]$  approximately. If we neglect the second term on the RHS of Eq. (11), and ignore the restriction that  $V^{\text{eff}}$  is hermitian, we have the trivial minimum  $M[V^{\text{eff}}] = 0$  at  $V^{\text{eff}} = V^{\text{ext}} + V^{\text{H}} + V^{\text{xc}}$  where  $V^{\text{xc}} = \sum_{ij} |\psi_i\rangle \Sigma(\varepsilon_j)_{ij} \langle \psi_j|$  and  $\Sigma(\varepsilon_j)_{ij} = \langle \psi_i | \Sigma(\varepsilon_j) | \psi_j \rangle$ . The second term is similarly minimum with  $\Sigma(\varepsilon_j) \rightarrow \Sigma(\varepsilon_i)$ . An average of the hermitian parts of these solutions results in

$$V^{\text{xc}} = \frac{1}{2} \sum_{ij} |\psi_i\rangle \{ \text{Re}[\Sigma(\varepsilon_i)]_{ij} + \text{Re}[\Sigma(\varepsilon_j)]_{ij} \} \langle \psi_j|. \quad \text{mode-A} \quad (13)$$

Eq. (13) is the same as Eq. (2) in Refs. [10] and [11]. We have derived Eq. (13) as an approximation to the exact minimization of  $M[V^{\text{eff}}]$ . Alternatively, we can take Eq. (13) as the definition of  $QSGW$ . We refer to Eq. (13) as ‘mode-A.’

The derivation  $V^{\text{eff}}$  above is reasonable but not unique; there can be other possible functionals  $M[V^{\text{eff}}]$  that result in different  $V^{\text{eff}}$ , or we might choose another approach to approximate the exact minimum  $M[V^{\text{eff}}]$ . It is instructive to evaluate the how results change when alternative choices are made for  $V^{\text{eff}}$ . In Ref. [10] we tested the following:

$$V^{\text{xc}} = \sum_i |\psi_i\rangle \text{Re}[\Sigma(\varepsilon_i)]_{ii} \langle \psi_i| + \sum_{i \neq j} |\psi_i\rangle \text{Re}[\Sigma(E_{\text{Fermi}})]_{ij} \langle \psi_j|. \quad \text{mode-B} \quad (14)$$

In this form (which we denote as ‘mode-B’), the off-diagonal elements are evaluated at  $E_{\text{Fermi}}$ . The diagonal parts of Eq. (14) and Eq. (13) are the same. As noted in Ref. [10], and as discussed in Sec. III, Eqs. (13) and (14) yield rather similar results, though we have found that mode-A results compare to experiment in the most systematic way.

Eq. (13) supplies the mapping  $V^{GW}(\omega) \rightarrow V^{\text{eff}}$  necessary to close the cycle. The  $QSGW$  cycle determines all  $H^0, V^{\text{eff}}, W$  and  $G$  self-consistently. As shown in Sec. III and also in Refs. [10, 11, 12],  $QSGW$  systematically overestimates semiconductor band gaps slightly, while the dielectric constant  $\epsilon_\infty$  is slightly too small [11]. After self-consistency attained, the eigenvalue problem

$(H^0 - \varepsilon_i)|\Psi_i\rangle = 0$  with  $V^{\text{eff}}$  given by Eq. (13) is the same as the eigenvalue problem that determines the QP eigenfunction, namely

$$\left[ \frac{-\nabla^2}{2m} + V^{\text{ext}} + V^{\text{H}} + \Sigma(E_i) - E_i \right] \psi_i = 0. \quad (15)$$

$E_i$  and  $\psi_i$  are the QPE's corresponding QP eigenfunctions. In other words, Eq. (13) can be taken as a way to modify the term  $\Sigma(E_i)$  to make it hermitian and index independent. Since the diagonal elements of  $\Sigma(E_i) - V^{\text{xc}}$  are zero and the off-diagonal elements that connect states with small energy differences are small,  $\Psi_i$  and  $\varepsilon_i$  for  $H^0$  are almost the same as the QP eigenfunction and eigenvalues given by Eq. (15). Thus the Fermi surface defined by  $G$  and  $G^0$  are almost the same as well.

Generating eigenfunctions from  $H^0$  is consistent with the Landau-Silin QP picture, discussed by, e.g., Pines and Nozieres in Sec. 3.3, Ref. [17]. We may call the independent-particle picture described by  $H^0$  as the *bare QP* picture. The *bare QP* interact with each other via the bare Coulomb interaction. The *bare QP* given by  $H^0$  evolve into the *dressed QP* interaction as  $\hat{H} - \hat{H}^0$  is turned on adiabatically. Here  $\hat{H}$  is total Hamiltonian (See Eq. (19)); and the ‘‘ signifies that  $\hat{H}$  is written in second quantized form.  $\hat{H}^0$  and  $H^0$  are equivalent. The *dressed QP* consists of the central *bare QP* and an induced polarization cloud consisting of other *bare QPs*; this view is compatible with the way interactions are treated in the GWA. We can use the *bare QP* by  $H^0$  in the Boltzmann-equation simulators, e.g., [18]. Note that  $\hat{H} - \hat{H}^0$  contains two kinds of contributions; not only the Coulomb interaction but also the term  $V^{\text{ext}} - V^{\text{eff}}$ . Along the adiabatic connection path we expect that the two contributions to the QP eigenfunctions will mostly cancel each other, namely, the condition ‘‘the *bare QP* eigenfunction  $\approx$  the *dressed QP* eigenfunction’’ is maintained (similarly for the eigenvalue). The adiabatic connection path defined in QSGW is better than the path in DFT where the eigenfunction of  $H_{\text{KS}}$  (Kohn-Sham Hamiltonian) evolved into the *dressed QP*. In the case of DFT,  $H^0$  is limited to the local potential, thus the physical quantities along the path can be not so stable. E.g, the band gap can change so much along the path (it can be metal to insulator in cases), even if it keeps the density along the path. [Note: terms bare QP and dressed QP here are used in a different meanings in Pines and Nozieres (Sec.1.6). They call QP as eigenstate of  $\hat{H}$  as ‘bare QP’, and spacially localized QP as ‘dressed QP’.]

Thus QSGW is physically reasonable, while the fully sc GW [19, 20] is not. From a theoretical point of view, the latter looks reasonable because it is derived from the Luttinger-Ward functional  $E[G]$ . This apparently keeps the symmetry on  $G$ , that is,  $E[G] = E[R[G]]$  where  $R[G]$  denotes some  $G \rightarrow G$  mapping (time translation, spacial translation, gauge transformation...); this clearly results in the conservation laws for external perturbations [21] because of the Noether's theorem. However, it contains

serious problems in practice. For example, fully sc GW uses  $W$  from  $\Pi = -iG \times G$ ; this includes the electron-hole excitations in its intermediate states with the weight of the product of renormalization factors  $Z \times Z$ . This is inconsistent with the expectation of the Landau's QP picture [10, 22]. In principle, such a deficiency should be recovered if you include higher order diagrams as Bechsted et al discussed [22, 23]. However, we can expect that such expansion series, where the lowest level of approximation is poor, should be not efficient expansion series.

Generally speaking, perturbation theories in the dressed Green's function  $G$  (as in Luttinger-Ward functional) can be very problematic because  $G$  contributes two different kinds of physical quantities to intermediate states: the QP part (suppressed by the factor  $Z$ ) and the incoherent part (e.g. plasmon-related satellites). Including the sum of ladder diagrams into  $\Pi$  via the Bethe-Salpeter equation, should be a poorer approximation if  $G$  is used instead of  $G^0$ , as it is in the RPA, because the one-particle part is suppressed by  $Z$  factors; also the contribution from the incoherent part can give physically meaningless contributions. The same can be said about the  $T$ -matrix treatment [24]. Such methods have clear physical interpretation in a quasiparticle framework, i.e. when the expansion is through  $G^0$ . A similar problem is encountered in theories such as ‘‘dynamical mean field theory’’+GW [25], where the local part of the proper polarization function is replaced with a ‘‘better’’ function which is obtained with the Anderson impurity model. This question, whether the perturbation should be based on  $G$ , or on  $G^0$ , also appeared when Hedin obtained an equation to determine the Landau QP parameters; See Eq. (26.12) in Ref.[2].

### C. Total energy

Once  $V^{\text{eff}}$  is given, we can calculate total energy based on the adiabatic connection formalism[26, 27, 28, 29]. Let us imagine an adiabatic connection path where the one-body Hamiltonian  $H^0 = \frac{-\nabla^2}{2m} + V^{\text{eff}}$  evolves into the total Hamiltonian  $\hat{H}$ , which is written as

$$\hat{H} = \hat{H}^{\text{k}} + \hat{V}^{\text{ee}} + \hat{V}^{\text{ext}}, \quad (16)$$

$$\hat{H}^{\text{k}} = \sum_{\sigma} \int d\mathbf{r} \hat{\psi}_{\sigma}^{\dagger}(\mathbf{r}) \left( -\frac{\nabla^2}{2m} \right) \hat{\psi}_{\sigma}(\mathbf{r}), \quad (17)$$

$$\hat{V}^{\text{ext}} = \sum_{\sigma} \int d\mathbf{r} V_{\sigma}^{\text{ext}}(\mathbf{r}) \hat{n}_{\sigma}(\mathbf{r}), \quad (18)$$

$$\hat{V}^{\text{ee}} = \frac{1}{2} \sum_{\sigma\sigma'} \int d\mathbf{r} d\mathbf{r}' v(\mathbf{r}, \mathbf{r}') \hat{\psi}_{\sigma}^{\dagger}(\mathbf{r}) \hat{\psi}_{\sigma'}^{\dagger}(\mathbf{r}') \hat{\psi}_{\sigma'}(\mathbf{r}') \hat{\psi}_{\sigma}(\mathbf{r})$$

$\hat{V}^{\text{ee}}$  is also defined with  $V^{\text{eff}}$  instead of  $V^{\text{ext}}$  in Eq. (18). We use standard notation for the field operators  $\hat{\psi}_{\sigma}(\mathbf{r})$ , spin index  $\sigma$ , and external potential  $V_{\sigma}^{\text{ext}}(\mathbf{r})$ . We omit spin indexes below for simplicity.

A path of adiabatic connection can be parametrized by  $\lambda$  as  $\hat{H}^\lambda = \hat{H}^0 + \lambda(\hat{V}^{\text{ext}} - \hat{V}^{\text{eff}} + \hat{V}^{\text{ee}})$ . Then the total

energy  $E$  is written as

$$E = E^0 + \int_0^1 d\lambda \frac{dE^\lambda}{d\lambda} = E^0 + \int_0^1 d\lambda \langle 0_\lambda | \hat{V}^{\text{ext}} - \hat{V}^{\text{eff}} | 0_\lambda \rangle + \int_0^1 d\lambda \langle 0_\lambda | \hat{V}^{\text{ee}} | 0_\lambda \rangle, \quad (20)$$

where  $|0_\lambda\rangle$  is the ground state for  $\hat{H}^\lambda$ . We define  $E^{\text{ext}} = \int_0^1 d\lambda \langle 0_\lambda | \hat{V}^{\text{ext}} | 0_\lambda \rangle$ . This path is different from the path used in DFT, where we take a path starting from  $\hat{H}_{\text{KS}}$  to  $\hat{H}$  while keeping the given density fixed. Along the path of the adiabatic connection, the Green's function changes from  $G^0$  to  $G$ . Because of our minimum-perturbation construction, Eq. (13), the QP parts (QP eigenfunction and QP eigenvalues) contained in  $G$  are well kept by  $G^0$ . If  $n_\lambda(\mathbf{r}) = \langle 0_\lambda | \hat{n}(\mathbf{r}) | 0_\lambda \rangle$  along the path it is almost the same as  $n_{\lambda=0}(\mathbf{r})$ ,  $E^0$  plus the second term in the RHS of Eq. (20) is reduced to be  $\langle 0_{\lambda=0} | \hat{H}^k + \hat{V}^{\text{ext}} | 0_{\lambda=0} \rangle$  (this is used in  $E^{\text{1st}}$  below). The last term on the RHS of Eq. (20) is given as  $E^{\text{H}} + E^{\text{x}} + E^{\text{c}}$ , where

$$E^{\text{H}} = \frac{1}{2} \int_0^1 d\lambda n_\lambda(\mathbf{r}) v(\mathbf{r}, \mathbf{r}') n_\lambda(\mathbf{r}'), \quad (21)$$

$$E^{\text{x}} = -\frac{1}{2} \int_0^1 d\lambda |n_\lambda(\mathbf{r}, \mathbf{r}')|^2 v(\mathbf{r}, \mathbf{r}'), \quad (22)$$

$$E^{\text{c}} = \frac{1}{2} \int_0^1 d\lambda \langle 0_\lambda | \hat{V}^{\text{ee}} | 0_\lambda \rangle - E^{\text{H}} - E^{\text{x}} \quad (23)$$

Here we used  $n_\lambda(\mathbf{r}, \mathbf{r}') = \langle 0_\lambda | \Psi^\dagger(\mathbf{r}) \Psi(\mathbf{r}') | 0_\lambda \rangle$ .

We define the 1st-order energy  $E^{\text{1st}}$  as the total energy neglecting  $E^{\text{c}}$ :

$$E^{\text{1st}} = E_0^{\text{k}} + E_0^{\text{ext}} + E_0^{\text{H}} + E_0^{\text{x}}, \quad (24)$$

where subscript 0 means that we use  $n_{\lambda=0}(\mathbf{r})$  instead of  $n_\lambda(\mathbf{r})$  (and same for  $n_\lambda(\mathbf{r}, \mathbf{r}')$ ) in the definition of  $E^{\text{ext}}$ ,  $E^{\text{H}}$  and  $E^{\text{x}}$ ;  $E_0^{\text{k}} = \langle 0_{\lambda=0} | \hat{H}^k | 0_{\lambda=0} \rangle$ . This is the HF-like total energy, but with the QP eigenfunctions given by  $V^{\text{eff}}$ .

$E^{\text{c}}$  is written as

$$E^{\text{c}} = \frac{1}{2} \int_0^1 d\lambda \text{Tr}[v \Pi_\lambda (1 - \lambda v \Pi_\lambda)^{-1} - v \Pi_\lambda], \quad (25)$$

where  $\Pi_\lambda$  is the proper polarization function for the ground state of  $\hat{H}^\lambda$ . The RPA makes the approximation  $\Pi_\lambda \approx \Pi_{\lambda=0}$  ( $\Pi_{\lambda=0}$  is simply expressed as  $\Pi$  below). The integral over  $\lambda$  is then trivial, and

$$\begin{aligned} E^{\text{c,RPA}} &= \frac{1}{2} \text{Tr}[-v \Pi + \log(1 - v \Pi)], \\ E^{\text{RPA}} &= E^{\text{1st}} + E^{\text{c,RPA}}, \end{aligned} \quad (26)$$

$E^{\text{RPA}}$  denotes the RPA total energy.  $\Pi$  is given by the product of non-interacting Green's functions  $\Pi =$

$-iG^0 \times G^0$ , where  $G^0$  is calculated from  $V^{\text{eff}}$ . Thus we have obtained the total energy expression  $E^{\text{RPA}}$  for QSGW.  $E^{\text{RPA}}$  will have characteristics missing in the LDA, e.g. physical effects owing to charge fluctuations such as the van der Waals interaction, the mirror force on metal surfaces, the activation energy, and so on. However, the calculation of  $E^{\text{c,RPA}}$  is numerically very difficult, because so many unoccupied states are needed. Also deeper states can couple to rather high-energy bands in the calculation of  $\Pi$ . Few calculations have been carried out to date[26, 27, 30, 31]. As far as we tested within our implementation, avoiding systematic errors is rather difficult. For example, when we change lattice constant,  $E^{\text{c,RPA}}$  artificially changes just because of the changes in the basis sets. This is a general problem of the RPA correlation energy.

Satisfying the self-consistency in QSGW may be not sufficient to determine the ground state uniquely. QSGW with Eq. (13) or Eq. (14) can result in multiple self-consistent solutions for  $G^0$ . This situation can occur even in HF theory. Thus we need to introduce a new assumption that ‘‘the ground state picked up is the state with lowest total energy’’. In other words, our method is the total energy minimization of  $E^{\text{RPA}}$  under the constraint of Eq. (13) (or Eq. (14)) in the determination of  $V^{\text{eff}}$ . However, in all cases shown in Sec.III, we obtain unique solutions (no multiple solutions) with Eq. (13) or Eq. (14). In a few cases studied so far, multiple solutions have been found, e.g. in GdN and YH<sub>3</sub> [13, 32]. These cases are related to the metal-insulator transition, as we will detail elsewhere. When seeking multiple solutions, we can propose a variation of QSGW, which is to add a local static one-particle potential as correction to Eq. (13). the potential is controlled to minimize  $E^{\text{RPA}}$ . This is a kind of hybridization of QSGW with the optimized effective potential method [28].

Some physical quantities can be calculated from  $G$  and from  $E^{\text{RPA}}[V^{\text{ext}}]$  independently, and the results need not be the same. The electron density is such an example. Let us check how they can differ. First of all, note  $E^{\text{RPA}}$  is given as a functional of  $V^{\text{ext}}$ , thus we can write it as  $E^{\text{RPA}}[V^{\text{ext}}]$ . Its functional derivative with respect to  $V^{\text{ext}}$  should give the density  $n(\mathbf{r})$  as  $n = \frac{\delta E^{\text{RPA}}}{\delta V^{\text{ext}}}$ . It is written as

$$n(\mathbf{r}) = \frac{\delta E^{\text{RPA}}}{\delta V^{\text{ext}}} = n^{G^0}(\mathbf{r}) - i \int d1 \int d2 (\Sigma^c(1, 2) - \bar{\Sigma}^c(1, 2)) \frac{\delta G^0(1, 2)}{\delta V^{\text{ext}}(\mathbf{r})}, \quad (27)$$

where  $n^{G^0}(\mathbf{r}) = -i \int d\omega G^0(\mathbf{r}, \mathbf{r}, \omega) e^{i\delta\omega}$  is the density for the non-interacting system with hamiltonian  $H^0$ .  $\bar{\Sigma}^c$  is a static version of correlated part of the self-energy  $\Sigma^c$  defined in the same manner as Eq. (13). Thus we expect the difference between  $n$  and  $n^{G^0}$  to be small. Alternatively, the density calculated from  $G$  as  $n^G = \int G(\mathbf{r}, \mathbf{r}, \omega) e^{i\delta\omega}$  is

$$n^G(\mathbf{r}) = n^{G^0}(\mathbf{r}) - i \int d1 \int d2 (\Sigma^c(1, 2) - \bar{\Sigma}^c(1, 2)) \frac{\delta G(1, 2)}{\delta V^{\text{ext}}(\mathbf{r})}. \quad (28)$$

These expressions differ only in the last factor. Since we can take  $G^0$  as a good substitute for  $G$ , we expect Eq. (27) and Eq. (28) give almost the same density. The total number of electrons calculated from  $G$  and from  $G^0$  are not necessarily the same, because  $GWA$  is not conserving[33, 34]. However, self-consistency that minimizes the difference between  $G$  and  $G^0$  means that the difference in the corresponding densities is also minimized.

## II. GW METHODOLOGICAL DETAILS

### A. Overview

In the full-potential linear muffin-tin orbital method (FP-LMTO) and its generalizations, eigenfunctions are expanded in linear combinations of Bloch summed muffin-tin orbitals (MTO)  $\chi_{\mathbf{R}Lj}^{\mathbf{k}}(\mathbf{r})$  of wave vector  $\mathbf{k}$  as

$$\Psi_{\mathbf{k}n}(\mathbf{r}) = \sum_{\mathbf{R}Lj} z_{\mathbf{R}Lj,n}^{\mathbf{k}} \chi_{\mathbf{R}Lj}^{\mathbf{k}}(\mathbf{r}), \quad (29)$$

$n$  is the band index;  $\Psi_{\mathbf{k}n}(\mathbf{r})$  is defined by the (eigenvector) coefficients  $z_{\mathbf{R}Lj,n}^{\mathbf{k}}$  and the shape of the  $\chi_{\mathbf{R}Lj}^{\mathbf{k}}(\mathbf{r})$ . The MTO we use here is a generalization of the usual LMTO basis, and is detailed in Refs.[9, 35].  $\mathbf{R}$  identifies the site where the MTO is centered,  $L$  identifies the angular momentum of the site. There can be multiple orbitals per  $\mathbf{R}L$ ; these are labeled by  $j$ . Inside a MT centered at  $\mathbf{R}$ , the radial part of  $\chi$  is spanned by radial functions ( $\varphi_{Rl}$ ,  $\dot{\varphi}_{Rl}$  or  $\varphi_{Rl}$ ,  $\dot{\varphi}_{Rl}$ ,  $\varphi_{Rl}^z$ ) at that site. Here  $\varphi_{Rl}$  is the solution of the radial Schrödinger equation at some energy  $\epsilon_\nu$  (usually, for  $l$  channels with some occupancy, this is chosen to be at the center of gravity for occupied states).  $\dot{\varphi}_{Rl}$  denotes the energy-derivative of  $\varphi_{Rl}$ ;  $\varphi_{Rl}^z$  denotes local orbitals, which are solutions to the radial wave equation at energies well above or well below  $\epsilon_\nu$ . We usually use two or three MTO's for each  $l$  for valence electrons (we use just one MTO for high  $l$  channels with almost zero occupancy). In any case these radial functions are represented in a compact notation  $\{\varphi_{Ru}\}$ .  $u$  is a compound index labeling  $L$  and one of the  $(\varphi_{Rl}, \dot{\varphi}_{Rl}, \varphi_{Rl}^z)$  triplet. The interstitial is comprised

of linear combinations of envelope functions consisting of smooth Hankel functions, which can be expanded in terms of plane waves[36].

Thus  $\Psi_{\mathbf{k}n}(\mathbf{r})$  in Eq. (29) can be written as a sum of augmentation and interstitial parts

$$\Psi_{\mathbf{k}n}(\mathbf{r}) = \sum_{Ru} \alpha_{Ru}^{\mathbf{k}n} \varphi_{Ru}^{\mathbf{k}}(\mathbf{r}) + \sum_{\mathbf{G}} \beta_{\mathbf{G}}^{\mathbf{k}n} P_{\mathbf{G}}^{\mathbf{k}}(\mathbf{r}), \quad (30)$$

where the interstitial plane wave (IPW) is defined as

$$P_{\mathbf{G}}^{\mathbf{k}}(\mathbf{r}) = \begin{cases} 0 & \text{if } \mathbf{r} \in \text{any MT} \\ \exp(i(\mathbf{k} + \mathbf{G}) \cdot \mathbf{r}) & \text{otherwise} \end{cases} \quad (31)$$

and  $\varphi_{Ru}^{\mathbf{k}}$  are Bloch sums of  $\varphi_{Ru}$

$$\varphi_{Ru}^{\mathbf{k}}(\mathbf{r}) \equiv \sum_{\mathbf{T}} \varphi_{Ru}(\mathbf{r} - \mathbf{R} - \mathbf{T}) \exp(i\mathbf{k} \cdot \mathbf{T}). \quad (32)$$

$\mathbf{T}$  and  $\mathbf{G}$  are lattice translation vectors in real and reciprocal space, respectively. Eq. (30) is equally valid in a LMTO or LAPW framework, and eigenfunctions from both types of methods have been used in this  $GW$  scheme [37, 38]. Here we restrict ourselves to (generalized) LMTO basis functions, based on smooth Hankel functions.

Throughout this paper, we will designate eigenfunctions constructed from MTO's as VAL. Below them are the core eigenfunctions which we designate as CORE. There are two fundamental distinctions between VAL and CORE: first, the latter are constructed independently by integration of the spherical part of the LDA potential, and they are not included in the secular matrix. Second, the CORE eigenfunctions are confined to MT spheres[39]. CORE eigenfunctions are also expanded using Eq. (30) in a trivial manner ( $\beta_{\mathbf{G}}^{\mathbf{k}n} = 0$  and only one of  $\alpha_{Ru}^{\mathbf{k}n}$  is nonzero); thus the discussion below applies to all eigenfunctions, VAL and CORE. In order to obtain CORE eigenfunctions, we calculate the LDA Kohn-Sham potential for the density given by  $H^0$ , and then solve the radial Schrödinger equation. In other words, we substitute the nonlocal  $V^{\text{eff}}$  potential with its LDA counterpart to calculate CORE. More details for the core treatment are given in Sec. II B.

Through Eq. (30), products  $\Psi_{\mathbf{k}_1 n} \times \Psi_{\mathbf{k}_2 n'}$  can be expanded by  $P_{\mathbf{G}}^{\mathbf{k}_1 + \mathbf{k}_2}(\mathbf{r})$  in the interstitial region because  $P_{\mathbf{G}_1}^{\mathbf{k}_1}(\mathbf{r}) \times P_{\mathbf{G}_2}^{\mathbf{k}_2}(\mathbf{r}) = P_{\mathbf{G}_1 + \mathbf{G}_2}^{\mathbf{k}_1 + \mathbf{k}_2}(\mathbf{r})$ . Within sphere  $R$ , wave function products can be expanded by  $B_{Rm}^{\mathbf{k}_1 + \mathbf{k}_2}(\mathbf{r})$ , which is the Bloch sum of the product basis (PB)  $\{B_{Rm}(\mathbf{r})\}$ , which in turn is constructed from the set of products  $\{\varphi_{Ru}(\mathbf{r}) \times \varphi_{Ru'}(\mathbf{r})\}$ . For the latter we adapted and improved the procedure of Aryasetiawan[40].

As detailed in Sec. II C, we define the mixed basis  $\{M_I^{\mathbf{k}}(\mathbf{r})\} \equiv \{P_{\mathbf{G}}^{\mathbf{k}}(\mathbf{r}), B_{Rm}^{\mathbf{k}}(\mathbf{r})\}$ , where the index  $I \equiv \{\mathbf{G}, Rm\}$  classifies the members of the basis. By construction,  $M_I^{\mathbf{k}}$  is a virtually complete basis, and efficient one for the expansion of  $\Psi_{\mathbf{k}n}$  products. Complete information to generate the  $GWA$  self-energy are matrix elements  $\langle \Psi_{\mathbf{q}n} | \Psi_{\mathbf{q}-\mathbf{k}n'} M_I^{\mathbf{k}} \rangle$ , the eigenvalues  $\varepsilon_{\mathbf{k}n}$ , the Coulomb matrix  $v_{IJ}(\mathbf{k}) \equiv \langle M_I^{\mathbf{k}} | v | M_J^{\mathbf{k}} \rangle$ , and the overlap

matrix  $\langle M_I^{\mathbf{k}} | M_J^{\mathbf{k}} \rangle$ . (The IPW overlap matrix is necessary because  $\langle P_{\mathbf{G}}^{\mathbf{k}} | P_{\mathbf{G}'}^{\mathbf{k}} \rangle \neq 0$  for  $\mathbf{G} \neq \mathbf{G}'$ .) The Coulomb interaction is expanded as

$$v(\mathbf{r}, \mathbf{r}') = \sum_{\mathbf{k}, I, J} |\tilde{M}_I^{\mathbf{k}}\rangle v_{IJ}(\mathbf{k}) \langle \tilde{M}_J^{\mathbf{k}}|, \quad (33)$$

where we define

$$|\tilde{M}_I^{\mathbf{k}}\rangle \equiv \sum_{I'} |M_{I'}^{\mathbf{k}}\rangle (O^{\mathbf{k}})_{I'I}^{-1}, \quad (34)$$

$$O_{I'I}^{\mathbf{k}} = \langle M_{I'}^{\mathbf{k}} | M_I^{\mathbf{k}} \rangle. \quad (35)$$

$W$  and the polarization function  $\Pi$  shown below are expanded in the same manner.

---

The exchange part of  $\Sigma$  is written in the mixed basis as

$$\langle \Psi_{\mathbf{q}n} | \Sigma_x | \Psi_{\mathbf{q}m} \rangle = - \sum_{\mathbf{k}}^{\text{BZ}} \sum_{n'}^{\text{occ}} \langle \Psi_{\mathbf{q}n} | \Psi_{\mathbf{q}-\mathbf{k}n'} \tilde{M}_I^{\mathbf{k}} \rangle v_{IJ}(\mathbf{k}) \langle \tilde{M}_J^{\mathbf{k}} \Psi_{\mathbf{q}-\mathbf{k}n'} | \Psi_{\mathbf{q}m} \rangle. \quad (36)$$

It is necessary to treat carefully the Brillouin zone (BZ) summation in Eq. (36) and also Eq. (39) because of the divergent character of  $v_{IJ}(\mathbf{k})$  at  $\mathbf{k} \rightarrow 0$ . It is explained in Sec. II E.

The screened Coulomb interaction  $W_{IJ}(\mathbf{q}, \omega)$  is calculated through Eq. (3), where the polarization function is written

$$\begin{aligned} \Pi_{IJ}(\mathbf{q}, \omega) &= \sum_{\mathbf{k}}^{\text{BZ}} \sum_n^{\text{occ}} \sum_{n'}^{\text{unocc}} \frac{\langle \tilde{M}_I^{\mathbf{q}} \Psi_{\mathbf{k}n} | \Psi_{\mathbf{q}+\mathbf{k}n'} \rangle \langle \Psi_{\mathbf{q}+\mathbf{k}n'} | \Psi_{\mathbf{k}n} \tilde{M}_J^{\mathbf{q}} \rangle}{\omega - (\varepsilon_{\mathbf{q}+\mathbf{k}n'} - \varepsilon_{\mathbf{k}n}) + i\delta} \\ &+ \sum_{\mathbf{k}}^{\text{BZ}} \sum_n^{\text{unocc}} \sum_{n'}^{\text{occ}} \frac{\langle \tilde{M}_I^{\mathbf{q}} \Psi_{\mathbf{k}n} | \Psi_{\mathbf{q}+\mathbf{k}n'} \rangle \langle \Psi_{\mathbf{q}+\mathbf{k}n'} | \Psi_{\mathbf{k}n} \tilde{M}_J^{\mathbf{q}} \rangle}{-\omega - (\varepsilon_{\mathbf{k}n} - \varepsilon_{\mathbf{q}+\mathbf{k}n'}) + i\delta}. \end{aligned} \quad (37)$$

When time-reversal symmetry is assumed,  $\Pi$  can be simplified to read

$$\begin{aligned} \Pi_{IJ}(\mathbf{q}, \omega) &= \sum_{\mathbf{k}}^{\text{BZ}} \sum_n^{\text{occ}} \sum_{n'}^{\text{unocc}} \langle \tilde{M}_I^{\mathbf{q}} \Psi_{\mathbf{k}n} | \Psi_{\mathbf{q}+\mathbf{k}n'} \rangle \langle \Psi_{\mathbf{q}+\mathbf{k}n'} | \Psi_{\mathbf{k}n} \tilde{M}_J^{\mathbf{q}} \rangle \\ &\times \left( \frac{1}{\omega - \varepsilon_{\mathbf{q}+\mathbf{k}n'} + \varepsilon_{\mathbf{k}n} + i\delta} - \frac{1}{\omega + \varepsilon_{\mathbf{q}+\mathbf{k}n'} - \varepsilon_{\mathbf{k}n} - i\delta} \right). \end{aligned} \quad (38)$$

We developed two kinds of tetrahedron method for the Brillouin zone (BZ) summation entering into  $\Pi$ . One follows the technique of Rath and Freeman [41]. The other, which we now mainly use, first calculates the imaginary part (more precisely the anti-hermitian part) of  $\Pi$ , and determines the real part via a Hilbert transformation (Kramers-Krönig relation); see Sec. II D.

The Hilbert transformation approach significantly reduces the computational time needed to calculate  $\Pi$  when a wide range of  $\omega$  is needed. A similar method was developed by Miyake and Aryasetiawan [42].

The correlation part of  $\Sigma$  is

$$\begin{aligned} \langle \Psi_{\mathbf{q}n} | \Sigma_c(\omega) | \Psi_{\mathbf{q}m} \rangle &= \sum_{\mathbf{k}}^{\text{BZ}} \sum_{n'}^{\text{All}} \sum_{IJ} \langle \Psi_{\mathbf{q}n} | \Psi_{\mathbf{q}-\mathbf{k}n'} \tilde{M}_I^{\mathbf{k}} \rangle \langle \tilde{M}_J^{\mathbf{k}} \Psi_{\mathbf{q}-\mathbf{k}n'} | \Psi_{\mathbf{q}m} \rangle \\ &\times \int_{-\infty}^{\infty} \frac{id\omega'}{2\pi} W_{IJ}^c(\mathbf{k}, \omega') \frac{1}{-\omega' + \omega - \varepsilon_{\mathbf{q}-\mathbf{k}n'} \pm i\delta}. \end{aligned} \quad (39)$$

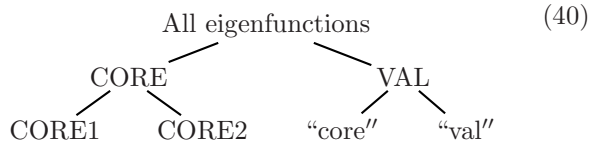
---

where  $W^c \equiv W - v$ ; and we must use  $-i\delta$  for occupied states and  $+i\delta$  for unoccupied states. Sec. II F explains

how the  $\omega$ -integration is performed.

### B. Core treatment

Contributions from core (or semi-core) eigenfunctions require special cares. In our *GW*, CORE is divided into groups, CORE1 and CORE2. Further, VAL can be divided into “core” and “val”. Thus all eigenfunctions are divided into the following groups



VAL can contain core eigenfunctions we denote as “core”. Such states are reliably determined by using local orbitals, tailored to these states[9]. For example, we can treat the Si  $2p$  core as “core”. States VAL=“core”+“val” are computed by the diagonalization of a secular matrix, they are completely orthogonal.

CORE1 is for deep core eigenfunctions. Their screening is small, and thus can be treated as exchange-only core. Based on the division of CORE according to Eq. (40), we evaluate  $\Sigma$  as

$$\Sigma = \Sigma_x^{\text{CORE1}} + \Sigma_x^{\text{CORE2+VAL}} + \Sigma_c^{\text{CORE2+VAL}}. \quad (41)$$

We generate two kinds of PB; one for  $\Sigma_x^{\text{CORE1}}$ , the other for CORE2+VAL. As explained in Sec. II C, these PB should be chosen taking into account what combination of eigenfunction products are important. States CORE2+VAL are usually included in  $\Pi$ , which determines  $W$ . Core eigenfunctions sufficiently deep (more than  $\sim 2$  Ry below  $E_F$ ), are well-localized within their MT spheres. For such core eigenfunctions, we confirmed that results are little affected by the kind of core treatment (CORE1, CORE2, and “core” are essentially equivalent); see Ref. [9].

As concerns their inclusion in the generation of  $\Pi$  and  $\Sigma$ , Eq. (41) means that not only VAL but also CORE2 are treated on the same footing as “val”. However, we have found that it is not always possible to reliably treat shallow cores (within  $\sim 2$  Ry below  $E_F$ ) as CORE2. Because CORE states are solved separately, the orthogonality to VAL is not perfect; this results in a small but uncontrollable error. The nonorthogonality problem is clearly seen in  $v\Pi(\mathbf{q}, \omega)$  as  $q \rightarrow 0$ : cancellation between denominator and numerator becomes imperfect. (We also implemented a procedure that enforced orthogonalization to VAL, but it would sometimes produce unphysical shapes in the core eigenfunctions.) Even in LDA calculations, MT spheres can be often too small to fully contain a shallow core’s eigenfunction. Thus we now usually do not use CORE2; for such shallow cores, we usually treat it as “core”  $\in$  VAL; or as CORE1 when they are deep

enough. We have carefully checked and confirmed the size of contributions from cores by changing such grouping, and also intentional cutoff of the core contribution to  $W$  and so on; see Ref. [9].

### C. Mixed basis for the expansion of $\Psi \times \Psi$

A unique feature of our *GW* implementation is its mixed basis set. This basis, which is virtually complete for the expansion of the products  $\Psi \times \Psi$ , is central for the efficient expansion of products of relatively localized functions, and essential for proper treatment of very localized states such as core states or  $f$  systems. Products within a MT sphere are expanded by the PB procedure originally developed by Aryasetiawan [40]. We use an improved version explained here. For the PB construction we start from the set of radial functions  $\{\phi_{ls}(r)\}$ , which are used for the augmentation for  $\Psi$  in a MT site.  $l$  is the principal angular momentum,  $s$  is the other index (e.g. we need  $s = 1$  for  $\phi$ , and  $s = 2$  for  $\dot{\phi}$  in addition to  $s = 3, 4, \dots$  for local orbitals and cores). The products  $\phi_{ls}(r) \times \phi_{l's'}(r)$  can be re-ordered by the total angular momentum  $l_p = l + l', \dots, |l - l'|$ . Then we radial product functions arranged by  $l_p$ . To make the computation efficient, we need to reduce the size of the radial product space, which we do as follows:

- (1) Restrict the choice of possible combinations  $\phi_{ls}(r)$  and  $\phi_{l's'}(r)$ . In the calculation of  $W$ , one  $\phi$  is used for occupied states, the other for unoccupied states [40]. In the calculation of  $\langle \Psi_{\mathbf{k}n'} | G \times W | \Psi_{\mathbf{k}n} \rangle$ ,  $\Psi_{\mathbf{k}m}^* \times \Psi_{\mathbf{k}n}$  appears, with  $\Psi_{\mathbf{k}m}^*$  coming from  $G$ . Thus all possible products can appear; however, we expect the important contributions come from low energy parts. Thus, we define two sets  $\Phi_{\text{OCC}}$  and  $\Phi_{\text{UNOCC}}$  as the subset of  $\{\phi_{ls}(r)\}$ .  $\Phi_{\text{OCC}}$  includes  $\phi_{ls}(r)$  mainly for occupied states (or a little larger sets), and  $\Phi_{\text{UNOCC}}$  is  $\Phi_{\text{OCC}}$  plus some  $\phi_{ls}(r)$  for unoccupied states (thus  $\Phi_{\text{OCC}} \in \Phi_{\text{UNOCC}}$ ). Then we take all possible products of  $\phi_{ls}(r) \times \phi_{l's'}(r)$  for  $\phi_{ls}(r) \in \Phi_{\text{OCC}}$  and  $\phi_{l's'}(r) \in \Phi_{\text{UNOCC}}$ . Following Aryasetiawan [40], we usually do not include  $\dot{\phi}$ -kinds of radial functions in these sets (we have checked in a number of cases that their inclusion contributes little).
- (2) Restrict  $l_p$  to be less than some cutoff  $l_p^{\text{MAX}}$ . We remove expensive product basis with high  $l_p$ . In our experience, we need  $l_p^{\text{MAX}} = 2 \times$  (maximum  $l$  with non-zero (or not too small) electron occupancy) is sufficient to predict band gaps to  $\sim 0.1\text{eV}$ , e.g. we need to take  $l_p^{\text{MAX}} = 4$  for transition metals.
- (3) Reduce linear dependency in the radial product basis. For each  $l_p$ , we have several radial product functions. We calculate the overlap matrix, make orthogonalized radial functions from them, and omit the subspace whose overlap eigenvalues

are smaller than some specified tolerance. The tolerance for each  $l_p$  can be different, and typically tolerances for higher  $l_p$  can be coarser than for lower  $l_p$ .

This procedure yields a product basis,  $\sim 100$  to  $150$  functions for a transition metal atom, and less for simple atoms (see Sec. III A for GaAs).

There are two kinds of cutoffs in the IPW part of the mixed basis:  $|\mathbf{q} + \mathbf{G}|_{\text{Max}}^{\Psi}$  for eigenfunctions Eq. (30), and  $|\mathbf{q} + \mathbf{G}|_{\text{Max}}^W$  for the expansion of  $W$ . In principle,  $|\mathbf{q} + \mathbf{G}|_{\text{Max}}^W$  must be  $2 \times |\mathbf{q} + \mathbf{G}|_{\text{Max}}^{\Psi}$  to span the Hilbert space of products. However, it is too expensive. The computational time is strongly controlled by the size of the mixed basis. Thus we usually take small  $|\mathbf{q} + \mathbf{G}|_{\text{Max}}^W$ , rather smaller than  $|\mathbf{q} + \mathbf{G}|_{\text{Max}}^{\Psi}$  (the computational time is not so strongly controlled by  $|\mathbf{q} + \mathbf{G}|_{\text{Max}}^{\Psi}$ ). As we illustrate in Sec. III A,  $\sim 0.1$  eV level accuracy can be realized for cutoffs substantially below  $2 \times |\mathbf{q} + \mathbf{G}|_{\text{Max}}^{\Psi}$ .

For the exchange part of CORE1, we need to construct another PB. It should include products of CORE1 and VAL. We construct it from  $\phi_{\text{CORE1}} \times \psi_{\text{VAL}}$ , where  $\psi_{\text{VAL}} \in \Phi_{\text{UNOCC}}$ , so as to make it safer ( $\Phi_{\text{OCC}}$  is bigger than  $\Phi_{\text{UNOCC}}$ ).

We also have tested other kinds of mixed basis which are smoothly augmented; we augment IPW's and con-

struct smoothed product basis (value and slope vanishing at the MT boundary). However, little computational advantage was realized for such a mixed basis.

#### D. Tetrahedron method for $W$

Eq. (37) requires an evaluation of this type of BZ integral;

$$X(\omega) = \sum_{\mathbf{k}} T_{\mathbf{k}} \frac{f(\varepsilon_a(\mathbf{k}))[1 - f(\varepsilon_b(\mathbf{k}))]}{\omega - (\varepsilon_b(\mathbf{k}) - \varepsilon_a(\mathbf{k})) \pm i\delta}, \quad (42)$$

where  $T_{\mathbf{k}}$  is a matrix element and  $f(\varepsilon)$  is the Fermi function. To evaluate this integral in the tetrahedron method, we divide the BZ into tetrahedra.  $T_{\mathbf{k}}$  is replaced with its average at the four corner of  $\mathbf{k}$ ,  $\overline{T}_{\mathbf{k}}$ . We evaluate the integral within a tetrahedron, linearly interpolating  $\varepsilon_a(\mathbf{k})$  and  $\varepsilon_b(\mathbf{k})$  between the four corners of the tetrahedron. In the metal case, we have to divide the tetrahedra into smaller tetrahedra; in each of them,  $f(\varepsilon_a(\mathbf{k}))[1 - f(\varepsilon_b(\mathbf{k}))] = 1$  or  $0$  are satisfied; see Ref. [41]. Thus we only pick up the smaller tetrahedron  $\Delta\Omega$  satisfying  $f(\varepsilon_a(\mathbf{k}))[1 - f(\varepsilon_b(\mathbf{k}))] = 1$  and calculate

$$\frac{1}{\pi} \text{Im} \Delta X(\omega) = \overline{T}_{\mathbf{k}} \int_{\Delta\Omega} d^3k \delta(\omega - (\varepsilon_b(\mathbf{k}) - \varepsilon_a(\mathbf{k}))), \quad (43)$$

Based on the assumption of linear interpolation, the integral in  $\text{Im} \Delta X(\omega)$  equals the area of the cross section of tetrahedron in a plane specified by energy  $\omega = (\varepsilon_b(\mathbf{k}) - \varepsilon_a(\mathbf{k}))$ . We create a histogram of energy windows  $[\omega(i), \omega(i+1)]$ ,  $i = 0, 1, \dots$ , by calculating the weight falling in each window as  $\int_{\omega(i)}^{\omega(i+1)} \text{Im} \Delta X(\omega) d\omega$ . We take windows specified as  $\omega(i) = a i + b i^2$  ( $i = 0, 1, \dots$ ), where we typically take  $a \sim 0.05$  eV and  $b \sim 1 - 10$  eV. Summing over contributions from all tetrahedra, we finally have

$$\text{Im} X([\omega(i), \omega(i+1)]) = \int_{\omega(i)}^{\omega(i+1)} d\omega \text{Im} X(\omega) = \sum_{\mathbf{k}} w_{\mathbf{k}}(i) T_{\mathbf{k}}. \quad (44)$$

Applying this scheme to Eq. (38), we have

$$\text{Im} \Pi(q, [\omega(i), \omega(i+1)]) = \sum_{\mathbf{k}} \sum_{n, n'} w_{\mathbf{k}}^{\mathbf{q}nn'}(i) T_{\mathbf{k}}^{\mathbf{q}nn'IJ}, \quad (45)$$

where  $T_{\mathbf{k}}^{\mathbf{q}nn'IJ} = \langle \tilde{M}_J^{\mathbf{q}} \Psi_{\mathbf{k}n} | \Psi_{\mathbf{q}+\mathbf{k}n'} \rangle \langle \Psi_{\mathbf{q}+\mathbf{k}n'} | \Psi_{\mathbf{k}n} \tilde{M}_J^{\mathbf{q}} \rangle$ . The real part of  $\Pi$  is calculated through a Hilbert transform of  $\text{Im} \Pi$  (Kramers-Krönig relation).

Some further considerations are as follows.

(A) For band index  $n$ ,  $\varepsilon_{\mathbf{k}n}$  may be degenerate. When it occurs, we merely symmetrize  $w_{\mathbf{k}}^{\mathbf{q}nn'}(i)$  with respect to the degenerate  $\varepsilon_{\mathbf{k}n}$ .

(B) When Eq. (37) is evaluated without time-reversal symmetry assumed, windows for negative energy must

be included because  $\text{Im} \Pi(q, -\omega) \neq \text{Im} \Pi(q, \omega)$ .

(C) In some limited tests, we found that linearly interpolating  $T_{\mathbf{k}}$  within the tetrahedron, instead of using  $\overline{T}_{\mathbf{k}}$ , did little to improve convergence.

(D) We sometimes use a ‘‘multi-divided’’ tetrahedron scheme to improve on the resolution of the energy de-

nominator. We take a doubled  $\mathbf{k}$ -mesh when generating  $w_{\mathbf{k}}^{\mathbf{q}nn'}(i)$ . For example, we calculate  $\Pi$  with a  $4 \times 4 \times 4$   $\mathbf{k}$ -mesh for  $k$  sum in Eq. (45); but we use a  $8 \times 8 \times 8$  mesh when we calculate  $w_{\mathbf{k}}^{\mathbf{q}nn'}(i)$ . Then the improvement of  $\Pi$  is typically intermediate between the two meshes: we obtain results between the  $4 \times 4 \times 4$  and  $8 \times 8 \times 8$  results in the original method.

### E. Brillouin-zone integral for the self-energy; the smearing method and the offset- $\Gamma$ method.

#### 1. Smearing method

To calculate  $\Sigma_x$  and  $\Sigma_c$ , Eqs. (36) and (39), each pole at  $\varepsilon_{\mathbf{q}-\mathbf{k}n'}$  is slightly smeared. The imaginary part, pro-

portional to  $\delta(\omega - \varepsilon_{\mathbf{q}-\mathbf{k}n'})$ , is broadened by a smeared function  $\bar{\delta}(\omega - \varepsilon_{\mathbf{q}-\mathbf{k}n'})$ . In order to treat metals, this smearing procedure is necessary. Usually we use a Gaussian for the smeared function

$$\bar{\delta}(\omega) = \frac{1}{\sqrt{2\pi}\sigma} \exp\left(-\frac{\omega^2}{2\sigma^2}\right). \quad (46)$$

though other forms have been tested as well.

We explain the smearing procedure by illustrating it for  $\Sigma_x$ . Eq. (36) becomes

$$\langle \Psi_{\mathbf{q}n} | \Sigma_x | \Psi_{\mathbf{q}m} \rangle = \sum_{\mathbf{k}}^{\text{BZ}} \rho_{\mathbf{q}nm}(\mathbf{k}), \quad (47)$$

$$\rho_{\mathbf{q}nm}(\mathbf{k}) \equiv \sum_{n'}^{\text{all}} \sum_{IJ} \bar{\theta}(E_F - \varepsilon_{\mathbf{q}-\mathbf{k}n'}) \langle \Psi_{\mathbf{q}n} | \Psi_{\mathbf{q}-\mathbf{k}n'} \tilde{M}_I^{\mathbf{k}} \rangle v_{IJ}(\mathbf{k}) \langle \tilde{M}_J^{\mathbf{k}} \Psi_{\mathbf{q}-\mathbf{k}n'} | \Psi_{\mathbf{q}m} \rangle \quad (48)$$

where  $\bar{\theta}(\omega)$  is a smeared step function,  $d\bar{\theta}(\omega)/d\omega = \bar{\delta}(\omega)$ .

Owing to the non-analytic Fermi energy cutoff in the metals case,  $\rho_{\mathbf{q}nm}(\mathbf{k})$  may not vary smoothly with  $\mathbf{k}$ . Increasing  $\sigma$  smooths out  $\rho_{\mathbf{q}nm}(\mathbf{k})$ , making it more rapidly convergent in spacing between  $\mathbf{k}$ -points, at the expense of introducing a systematic error to the fully  $\mathbf{k}$ -converged result. With a denser  $\mathbf{k}$  mesh, smaller  $\sigma$  can be used, which reduces the systematic error. In practice we can obtain converged results for given  $\sigma$  with respect to the number of  $\mathbf{k}$  points, and then take the  $\sigma \rightarrow 0$  limit.

#### 2. Offset- $\Gamma$ method

The integrand in Eq. (47) contains divergent term proportional to  $1/|\mathbf{k}|^2$  for  $\mathbf{k} \rightarrow 0$ . In order to handle this

divergence we invented the offset- $\Gamma$  method. It was originally developed by ourselves[6] and is now used by other groups[43, 44]; it is numerically essentially equivalent to the method of Gygi and Baldereschi[45], where the divergent part is treated analytically.

We begin with the method of Gygi and Baldereschi[45]. The Coulomb interaction  $v_{IJ}(\mathbf{k})$ , which is a periodic function in  $\mathbf{k}$ , includes a divergent part  $v_{IJ}^0(\mathbf{k}) \propto U_I^0(\mathbf{k})U_J^{0*}(\mathbf{k})F(\mathbf{k})$  where  $F(\mathbf{k}) \rightarrow 1/|\mathbf{k}|^2$  as  $\mathbf{k} \rightarrow 0$ .  $U_I^0(\mathbf{k})$  are coefficients to plane wave  $e^{i\mathbf{k}\mathbf{r}}$  in the mixed basis expansion. They divided the integrand into two terms, one with no singular part which is treated numerically; the other a combination of analytic functions that contain the singular part:

$$\langle \Psi_{\mathbf{q}n} | \Sigma_x | \Psi_{\mathbf{q}m} \rangle = \sum_{\mathbf{k}}^{\text{BZ}} (\rho_{\mathbf{q}nm}(\mathbf{k}) - \rho_{\mathbf{q}nm}^0(\mathbf{k})) + A_{\mathbf{q}nm} \sum_{\mathbf{k}}^{\text{BZ}} F(\mathbf{k}), \quad (49)$$

where

$$\rho_{\mathbf{q}nm}^0(\mathbf{k}) = A_{\mathbf{q}nm} F(\mathbf{k}) \quad (50)$$

$$A_{\mathbf{q}nm} = \lim_{\mathbf{k} \rightarrow 0} |\mathbf{k}|^2 \rho_{\mathbf{q}nm}(\mathbf{k}). \quad (51)$$

As for the first term on the RHS of Eq. (49), the inte-

grand  $\rho_{\mathbf{q}nm}(\mathbf{k}) - \rho_{\mathbf{q}nm}^0(\mathbf{k})$  is a smooth function in the BZ

with no singularity (more precisely, it can contain a part like  $\propto k_x/|\mathbf{k}|^2$ , however, it adds zero contribution around  $\mathbf{k} = 0$  because it is odd in  $k$ ); it is thus easily evaluated numerically. The second term is analytically evaluated because  $F(\mathbf{k})$  is chosen to be an analytic function as shown below. We evaluate the first term by numerical integration on a discrete mesh in a primitive cell in the BZ. The mesh is given as

$$\mathbf{k}(i_1, i_2, i_3) = 2\pi\left(\frac{i_1}{N_1}\mathbf{b}_1 + \frac{i_2}{N_2}\mathbf{b}_2 + \frac{i_3}{N_3}\mathbf{b}_3\right) \quad (52)$$

$$\sum_{\mathbf{k}}^{\text{BZ}} \approx \frac{1}{N_1 N_2 N_3} \sum_{i_1, i_2, i_3}.$$

Forms of the analytic functions  $F(\mathbf{k})$  are chosen that can be analytically integrated. We choose  $F(\mathbf{k})$  as

$$F(\mathbf{k}) = \sum_{\mathbf{G}}^{\text{All}} \frac{\exp(-\alpha|\mathbf{q} + \mathbf{G}|^2)}{|\mathbf{q} + \mathbf{G}|^2}, \quad (53)$$

where  $\mathbf{G}$  denotes all the inverse reciprocal vectors and  $\alpha$  is a parameter.  $F(\mathbf{k})$  is positive definite, periodic in BZ and has the requisite divergence at  $\mathbf{k} \rightarrow 0$ . (Gygi and

Baldereschi used a different function in Ref. [45], but it satisfies the same conditions.) We can easily evaluate  $F(\mathbf{k})$  analytically. Thus it is possible to calculate  $\Sigma_x$  if we can obtain the coefficients  $A_{\mathbf{q}nm}$ . However, it is not easy to calculate  $A_{\mathbf{q}nm}$ . This is especially true for  $\Sigma_c$ , Eq. (39), where the coefficients are energy-dependent.

The offset- $\Gamma$  method avoids explicit evaluation of  $A_{\mathbf{q}nm}$ , while retaining accuracy essentially equivalent to the method described above. It evaluates the  $\mathbf{k}$ -integral in Eq. (47) as a discrete sum

$$\sum_{\mathbf{k}}^{\text{BZ}} \approx \frac{1}{N_1 N_2 N_3} \widetilde{\sum}_{i_1, i_2, i_3}, \quad (54)$$

where  $\widetilde{\sum}$  denotes the sum for  $\mathbf{k}(i_1, i_2, i_3)$  but  $\mathbf{k} = 0$  is replaced by the offset- $\Gamma$  point  $\mathbf{Q} = (Q, 0, 0)$ .  $\mathbf{Q}$  is near  $\mathbf{k} = 0$ , and chosen so as to integrate  $F(\mathbf{k})$  exactly:

$$\sum_{\mathbf{k}}^{\text{BZ}} F(\mathbf{k}) = \frac{1}{N_1 N_2 N_3} \widetilde{\sum}_{i_1, i_2, i_3} F(\mathbf{k}). \quad (55)$$

Then Eq. (47) becomes

$$\begin{aligned} \langle \Psi_{\mathbf{q}n} | \Sigma_x | \Psi_{\mathbf{q}m} \rangle &\approx \frac{1}{N_1 N_2 N_3} \widetilde{\sum}_{i_1, i_2, i_3} \rho_{\mathbf{q}nm}(\mathbf{k}) \\ &= \frac{1}{N_1 N_2 N_3} \widetilde{\sum}_{i_1, i_2, i_3} (\rho_{\mathbf{q}nm}(\mathbf{k}) - \rho_{\mathbf{q}nm}^0(\mathbf{k})) + \frac{A_{\mathbf{q}nm}}{N_1 N_2 N_3} \widetilde{\sum}_{i_1, i_2, i_3} F(\mathbf{k}). \end{aligned} \quad (56)$$

For larger  $N_1 N_2 N_3$ ,  $(Q, 0, 0)$  is closer to  $(0, 0, 0)$ , thus the first term on the RHS of Eq. (56) is little different from the sum with the mesh Eq. (52). Then the second term in Eq. (56) is exactly the same as the second term in Eq. (49) because of Eq. (55). Thus the simple sum  $\frac{1}{N_1 N_2 N_3} \widetilde{\sum}_{i_1, i_2, i_3}$  can reproduce the results given by the method Eq. (49).

In practical applications, we have to take some set of  $\mathbf{Q}$  points to preserve the crystal symmetry. Typically we prepare six  $\mathbf{Q}$  points,  $(\pm Q, 0, 0)$ ,  $(0, \pm Q, 0)$ ,  $(0, 0, \pm Q)$ ,

and then generate all possible points by the crystal symmetry. The weight for each  $\mathbf{Q}$  should be  $1/N_1 N_2 N_3$  divided by the total number of  $\mathbf{Q}$  points. The value of  $Q$  is chosen to satisfy Eq. (55). It evidently depends on the choice of  $F(\mathbf{k})$ ; in particular when  $F$  is given by Eq. (53),  $\mathbf{Q}$  depends on  $\alpha$ . A reasonable choice for  $\alpha$  is  $\alpha \rightarrow 0$  (then no external scale is introduced). However, we found  $\alpha = 1.0$  a.u. is small enough for simple solids, and the results depend little on whether  $\alpha = 1.0$  or  $\alpha \rightarrow 0$ .

In addition, we make the following approximation:

$$\rho_{\mathbf{q}n}(\mathbf{Q}) \approx \sum_{n'}^{\text{all}} \sum_{IJ} \bar{\theta}(E_F - \varepsilon_{\mathbf{q}n'}) \langle \Psi_{\mathbf{q}n} | \Psi_{\mathbf{q}n'} \tilde{M}_I^{\mathbf{k}=0} \rangle v_{IJ}(\mathbf{Q}) \langle \tilde{M}_J^{\mathbf{k}=0} \Psi_{\mathbf{q}n'} | \Psi_{\mathbf{q}n} \rangle. \quad (57)$$

That is, the matrix element is not evaluated at  $\mathbf{k} = \mathbf{Q}$  but

at  $\mathbf{k} = 0$ . This is not necessary, but it reduces the com-

putational costs and omits the contribution  $\propto k_x/|\mathbf{k}|^2$  which gives no contribution around  $\mathbf{k} = 0$ .

Finally, we use crystal symmetry to evaluate Eq. (48):  $v_{IJ}(\mathbf{k})$  and also  $W_{IJ}^c(\mathbf{k})$  are calculated only at the irreducible  $\mathbf{k}$  points and at the inequivalent offset- $\Gamma$  points.

We also tested a modified version of the offset- $\Gamma$  method with another kind of BZ mesh (it is not used for any results in this paper). The uniform mesh is shifted from the  $\Gamma$  point:

$$\mathbf{k}(i_1, i_2, i_3) = 2\pi \left( \frac{i_1 + \frac{1}{2}}{N_1} \mathbf{b}_1 + \frac{i_2 + \frac{1}{2}}{N_2} \mathbf{b}_2 + \frac{i_3 + \frac{1}{2}}{N_3} \mathbf{b}_3 \right) \quad (58)$$

Then we evaluate the BZ integral as

$$\sum_{\mathbf{k}}^{\text{BZ}} F(\mathbf{k}) \rightarrow \sum_{i_1, i_2, i_3} W_{\mathbf{k}} F(\mathbf{k}) + \frac{W_{\mathbf{Q}}}{N_1 N_2 N_3} F(\mathbf{Q}). \quad (59)$$

where  $\mathbf{k}(i_1, i_2, i_3)$  is used.  $W_{\mathbf{Q}}$  is a parameter given by hand to specify the weight for the offset- $\Gamma$  point  $\mathbf{Q}$ . We usually use a small value, e.g.,  $W_{\mathbf{Q}} \sim 0.01$  or less, but taken not too small so that it does not cause numerical problems. Integration weights are  $W_{\mathbf{k}} = 1/(N_1 N_2 N_3)$  except for those closest to  $\Gamma$ . These latter  $W_{(\text{shortest } \mathbf{k})}$  are chosen so that the sum of all  $W_{\mathbf{k}}$  and  $W_{\mathbf{Q}}$  is unity. Then  $\mathbf{Q}$  is determined in the same manner in the original offset- $\Gamma$  method. This scheme picks up the divergent part of integral correctly, and can be advantageous in some cases, in particular for oddly shaped Brillouin zones.

The original method with Eq. (52) has difficulty in treating anisotropic systems like a one-dimensional atomic chain. In such a case, we can not determine reasonable  $\mathbf{Q}$  for the BZ division for, e.g., ( $N_1 = N_2 = 1$  and  $N_3 = \text{large number}$ ), while the modified form Eq. (Eq. (58)) has no difficulty. We can choose  $\mathbf{Q}$  close to  $\Gamma$  (any  $\mathbf{Q}$  can be chosen if it is close enough to  $\Gamma$ ). As  $W_{\mathbf{Q}}$  becomes smaller, so does  $\mathbf{Q}$ . Two final points relevant to the modified version are:

- In some anisotropic cases (e.g. anti-ferromagnetic II NiO), we need to use negative  $W_{\mathbf{Q}}$  because the shortest  $\mathbf{k}$  on regular mesh is already too short and the integral of  $F(\mathbf{q})$  evaluated on the mesh of Eq. (58) already exceeds the exact value. However, the modified version works even in such a case.

- In some cases (e.g. Si), the shifted mesh can be somewhat disadvantageous because certain symmetry operations can map some mesh points to new points not within the shifted mesh, Eq. (58). Then the obtained QP energies that are supposed to be degenerate are not precisely for numerical reasons. One solution is to take denser  $\mathbf{k}$  mesh to avoid the effect of discretization. Our current implementation allows us to compute  $\Pi$  and  $\Sigma$  with different meshes, Eq. (52) or Eq. (58). This is sometimes advantageous to check the stability of calculations with respect to the  $\mathbf{k}$  mesh.

#### F. $\omega'$ -integral for $\Sigma^c$

Eq. (39) contains the following integral

$$X = \int_{-\infty}^{\infty} \frac{id\omega'}{2\pi} W^c(\omega') \frac{1}{-\omega' + \omega_\varepsilon \pm i\delta}, \quad (60)$$

where  $\omega_\varepsilon = \omega - \varepsilon_{\mathbf{q}-\mathbf{k}n'}$ . Here we fix indexes  $I, J, \mathbf{k}, \mathbf{q}, n'$  and omit them for simplicity. We use a version of the imaginary-path axis integral method [46, 47]: the integration path is deformed from the real-axis to the imaginary axis in such a way that no poles are crossed; see Fig. 1. As a result,  $X$  is written as the sum of an imaginary axis integral  $X_{\text{img}}$  and pole contributions  $X_{\text{real}}$ .  $X_{\text{img}}$  is

$$X_{\text{img}} = \frac{-1}{\pi} \int_0^\infty d\omega' W_S(\omega') \frac{\omega_\varepsilon}{\omega'^2 + \omega_\varepsilon^2} + \frac{1}{\pi} \int_0^\infty d\omega' W_A(\omega') \frac{\omega'}{\omega'^2 + \omega_\varepsilon^2}, \quad (61)$$

where  $W_S(\omega') = [W^c(i\omega') + W^c(-i\omega')]/2$  and  $W_A(\omega') = [W^c(i\omega') - W^c(-i\omega')]/2i$ . Note that  $W_A(\omega') \neq 0$  unless time-reversal symmetry is satisfied.  $X_{\text{img}}$  adds a hermitian contribution to  $\Sigma^c$ .

We have to pay attention to the fact that  $W_S(\omega')$  is rather strongly peaked around  $\omega' = 0$ , and follow the prescription by Aryasetiawan [47] to evaluate the first term in Eq. (61):

(i) Divide  $W_S(\omega')$  into  $W_S(0) \exp(-a\omega'^2)$  and the residual,  $W_S(\omega') - W_S(0) \exp(-a\omega'^2)$ .  $a$  is a pa-

rameter. The first integral is performed analytically, the residual part numerically. We chose  $a$  in one of two ways, either to match  $d^2 W_S(\omega')/d\omega'^2$  at  $\omega' = 0$ , or use  $a = 1.0 \text{ a.u.}$  (as originally done by Aryasetiawan). Then we find the latter is usually good enough, in the sense that it does not impose additional burden on numerical integration of the residual term.

(ii) The residual term is integrated with a Gaussian quadrature in the interval  $x = [0, 1]$ , making the

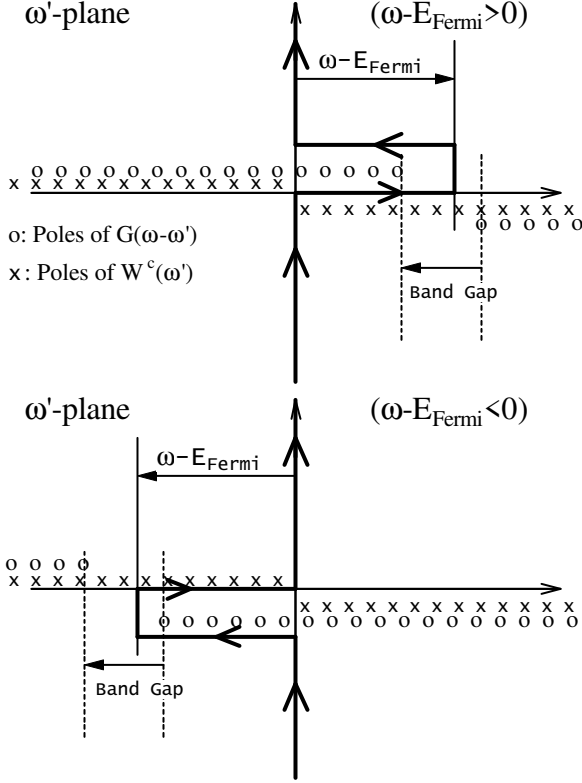


FIG. 1: Integration contour of the correlated part of the self-energy, Eq. (61). The original path along real axis is deformed without crossing poles.  $G(\mathbf{q} - \mathbf{k}, \omega - \omega') = \sum_n 1/(\omega - \omega' - \varepsilon_{\mathbf{q}-\mathbf{k}n})$  has poles at  $\omega' = \omega - \varepsilon_{\mathbf{q}-\mathbf{k}n}$ .

transformation  $\omega' = x/(1-x)$  a.u. Typically, a 6 point quadrature is sufficient to achieve convergence less than 0.01 eV in the band gap.

- (iii) We include an extra factor  $1 - \exp[-(\omega'^2 + \omega_\varepsilon^2)/2\alpha^2]$  in the integrand of the numerical integration. This avoids numerical difficulties, since  $\omega_\varepsilon/(\omega'^2 + \omega_\varepsilon^2)$  can be large. In our implementation, we simply fix  $\alpha$  in (iii) as same as  $\sigma$  for the smearing in Eq. (46) and check the convergence. Generally speaking,  $\sigma = 0.001$  a.u. give satisfactory results (differences are negligible compared to  $\sigma \rightarrow 0$  results).

$X_{\text{real}}$  has three branches

$$X_{\text{real}} = \begin{cases} W^c(\omega_\varepsilon) & \text{if } \omega - E_F > \omega_\varepsilon > 0 \\ -W^c(\omega_\varepsilon) & \text{if } 0 > \omega_\varepsilon > \omega - E_F \\ 0 & \text{otherwise} \end{cases} \quad (62)$$

Poles are smeared out as discussed in Sec. II E;  $\varepsilon_{\mathbf{q}-\mathbf{k}n'}$  (thus  $\omega_\varepsilon$ ) has a Gaussian distribution. This means that we take  $\pm wW^c(\bar{\omega}_\varepsilon)$  instead of Eq. (62), where  $w$  is the weight sum falling in the range  $[0, \omega - E_F]$  (or  $[\omega - E_F, 0]$ ), and  $\bar{\omega}_\varepsilon$  is the mean value of  $\omega_\varepsilon$  in the range. The QP

lifetime (which originates from the non-hermitian part of  $\Sigma^c$ ) comes entirely from the imaginary part of  $X_{\text{real}}$ . Thus the condition that the lifetime is infinite (no imaginary part) at  $\omega = E_F$  is assured from the path shown in Fig. 1, since  $\omega = E_F$  means no contour on real axis. The lifetime of a QP is due to its decay to another QP accompanied by the states included in  $\text{Im}[W^c]$ ; these states can be independent electron-hole excitations, plasmon-like collective modes, local collective charge oscillations (e.g.  $d$  electrons in transition metals oscillate with  $\sim 5$  eV [48]), and also their hybridization. In the insulator case, there is “pair-production threshold”: if the electron QPE is below (conduction band minimum)  $+ E_g$ , its imaginary part is zero because it can not decay to another electron accompanied by an electron-hole pair (similarly for holes). We will show results elsewhere; to calculate QPE lifetimes, a numerically careful treatment is necessary—especially for  $\text{Im}W^c$ .

### G. Self-consistency for $\Sigma$

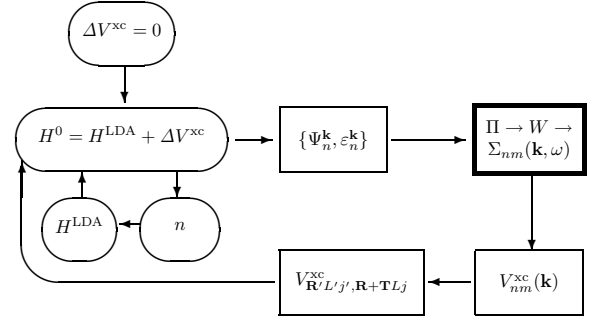


FIG. 2: Self-consistency cycle. Cycle consists of a large loop  $H^{\text{LDA}} + \Delta V^{\text{xc}} \rightarrow \Sigma(\mathbf{q}, \omega) \rightarrow V^{\text{xc}} \rightarrow H^{\text{LDA}} + \Delta V^{\text{xc}} \rightarrow \dots$ . There is an inner loop within the  $H^0 = H^{\text{LDA}} + \Delta V^{\text{xc}}$  step, where the density and LDA potential are made self-consistent for a fixed  $\Delta V^{\text{xc}}$ . The cycle is started by taking  $\Delta V^{\text{xc}} = 0$ , or  $H^0 = H^{\text{LDA}}$ ; it is equivalent to the standard  $G^{\text{LDA}}W^{\text{LDA}}$  with  $Z = 1$  and including the off-diagonal parts of  $\Sigma$ . The time-consuming part is framed in bold. Subscripts to  $\Sigma$  and  $V^{\text{xc}}$  refer to the basis it is represented in; see text.

The self-consistent cycle is shown in Fig. 2. It is initiated as in a standard  $GW$  calculation, by using  $H^{\text{LDA}}$  for  $H^0$  (“zerth iteration”). It is a challenge to calculate the QSGW  $V^{\text{xc}}$ , Eq. (13), efficiently. The most time-consuming part of a standard  $GW$  calculation is the generation of the polarization function,  $\Pi(\mathbf{q}, \omega)$ , because only diagonal parts of  $\Sigma$  are required. However in the QSGW case, the generation of  $\Sigma(\mathbf{q}, \omega)$  is typically 3 to 10 times more expensive computationally. These two steps together (bold frame, Fig. 2) are typically 100 to 1000 times more demanding computationally than the rest of the cycle. Once a new static  $V^{\text{xc}}$  is generated, the density is made self-consistent in a “small” loop where the

difference in the QSGW and LDA exchange-correlation potentials,  $\Delta V^{\text{xc}} \equiv V^{\text{xc}} - V^{\text{xc,LDA}}$ , is kept constant.  $V^{\text{xc}} - V^{\text{xc,LDA}}$  is expected to be somewhat less sensitive to density variations than  $V^{\text{xc}}$  itself, so the inner loop updates the density and Hartree potential in a way intended to minimize the number cycles needed to generate  $\Sigma$  self-consistently. That number depends on how good the LDA starting point is: for a simple semiconductor such as Si typically three or four iterations are enough for QP levels to be converged to 0.01 eV. The situation is very different for complex compounds such as NiO; the number of cycles then depends not only on the quality of the LDA starting point, but other complicating factors as well. In particular some fluctuations (spin and orbital moments) can be particularly low-energy, and require many iterations for self-consistency. Solutions near a transition to a competing electronic state are also difficult to converge.

$V^{\text{xc}}$  is calculated only at irreducible  $\mathbf{k}$ -points on the regular mesh, Eq. (52). However, we must evaluate  $\Delta V^{\text{xc}}(\mathbf{k})$  at continuous  $\mathbf{k}$ -points for a viable scheme. In the self-consistency cycle, for example, the offset- $\Gamma$

method requires eigenfunctions at other  $\mathbf{k}$ . The ability to generate  $H^0$  at any  $\mathbf{k}$  is also needed to generate continuous energy bands (essential for reliable determination of detailed properties of the band structure such as effective masses) or integrated quantities, e.g. DOS or EELS calculations. Also, while it is not essential, we typically use a finer  $\mathbf{k}$  mesh for the step in the cycle that generates the density and Hartree potential (oval loops in Fig. 2), than we do in the *GW* part of the cycle[49].

The interpolation is accomplished in the (generalized) LMTO basis by exploiting their finite range. Several transformations are necessary for a practical scheme, which we now describe. For a given density and  $\Delta V^{\text{xc}}(\mathbf{k})$  there are three kinds of basis sets: the MTO's  $\chi_{\mathbf{R}Lj}^{\mathbf{k}}$ ; the basis  $\Psi_{\mathbf{k}n}^{\text{LDA}}$  in which  $H^{\text{LDA}}(\mathbf{k})$  is diagonal (the ‘‘LDA’’ basis); and the basis  $\Psi_n^{\mathbf{k}}$  in which  $H^0 = H^{\text{LDA}}(\mathbf{k}) + \Delta V^{\text{xc}}(\mathbf{k})$  is diagonal (the ‘‘QSGW’’ basis). They are related by the linear transformation Eq. (29). For example  $\Delta V_{nm}^{\text{xc}}$  in the QSGW basis,  $\Delta V_{nm}^{\text{xc}}(\mathbf{k}) \equiv |\Psi_n^{\mathbf{k}}\rangle \Delta V^{\text{xc}}(\mathbf{k}) \langle \Psi_m^{\mathbf{k}}|$ , is related to  $\Delta V_{\mathbf{R}'L'j',\mathbf{R}Lj}^{\text{xc}}(\mathbf{k}) \equiv |\chi_{\mathbf{R}'L'j'}^{\mathbf{k}}\rangle \Delta V^{\text{xc}}(\mathbf{k}) \langle \chi_{\mathbf{R}Lj}^{\mathbf{k}}|$  in the MTO basis by

$$\Delta V_{nm}^{\text{xc}}(\mathbf{k}) = \sum_{\mathbf{R}'L'j',\mathbf{R}Lj} z_{\mathbf{R}'L'j',n}^{\mathbf{k}\dagger} \Delta V_{\mathbf{R}'L'j',\mathbf{R}Lj}^{\text{xc}}(\mathbf{k}) z_{\mathbf{R}Lj,m}^{\mathbf{k}} \quad (63)$$

$V^{\text{xc}}(\mathbf{k})$  is generated in the QSGW basis. Generally, interpolating  $V^{\text{xc}}(\mathbf{k})$  to other  $\mathbf{k}$  will be problematic in this basis, because of ambiguities near band-crossings. This problem must be avoided by transformation to the MTO basis. Thus, the transformation proceeds as:

$$V_{nm}^{\text{xc}}(\mathbf{k}) \rightarrow \Delta V_{nm}^{\text{xc}}(\mathbf{k}) \rightarrow \Delta V_{\mathbf{R}'L'j',\mathbf{R}Lj}^{\text{xc}}(\mathbf{k}) \rightarrow \Delta V_{\mathbf{R}'L'j',\mathbf{R}+\mathbf{T}Lj}^{\text{xc}}.$$

The LDA exchange-correlation potential is subtracted, and Eq. (63) is inverted to obtain  $\Delta V_{\mathbf{R}'L'j',\mathbf{R}Lj}^{\text{xc}}(\mathbf{k})$ . ( $z_{\mathbf{R}Lj,m}^{\mathbf{k}}$  is a square matrix in  $(\mathbf{R}Lj, m)$  since the number of eigenfunctions is the dimension of the Hilbert space.) The last step is an inverse Bloch transform of  $\Delta V_{\mathbf{R}'L'j',\mathbf{R}Lj}^{\text{xc}}(\mathbf{k})$  to real space. It is done by FFT techniques in order to exactly recover  $\Delta V_{\mathbf{R}'L'j',\mathbf{R}Lj}^{\text{xc}}(\mathbf{k})$  by the Bloch sum  $\sum_{\mathbf{T}} e^{i\mathbf{k}\cdot\mathbf{T}} \Delta V_{\mathbf{R}'L'j',\mathbf{R}+\mathbf{T}Lj}^{\text{xc}}$ . It is accomplished in practice by rotating  $\Delta V^{\text{xc}}$  according to the crystal symmetry to the mesh of  $\mathbf{k}$ -points in the full BZ, Eq. (52), and symmetrizing it using the available crystal symmetry operations.

Usually we calculate  $\Delta V_{nm}^{\text{xc}}(\mathbf{k})$  only for a subblock of the entire matrix, that is for  $(n, m)$  where  $\varepsilon_{\mathbf{k}n}, \varepsilon_{\mathbf{k}m} < E_{\text{xccut}}$ . Typically  $E_{\text{xccut}} \sim E_{\text{F}} + 2$  to  $E_{\text{F}} + 3.5$  Ry (larger values for wide-gap systems such as diamond). We approximate  $\Delta V_{nm}^{\text{xc}}(\mathbf{k})$  for the higher lying states by a matrix that is diagonal in the LDA basis. The diagonal elements are taken to be linear function of the corresponding LDA energy,  $\Delta V_{ii}^{\text{xc}}(\mathbf{k}) = a\varepsilon_i^{\text{LDA}} + b$ . The ‘ $\sim$ ’ over the subscripts signifies that the matrix is represented in the

basis of LDA eigenfunctions, not QSGW eigenfunctions. (It is computationally inconvenient to add the diagonal term in the QSGW basis. There is no formal reason to prefer one basis over the other, and it matters little which is taken in any case.)  $a$  and  $b$  are determined by fitting them to  $\Delta V_{ii}^{\text{xc}}(\mathbf{k})$  which are initially generated by a test calculation with somewhat larger  $E_{\text{xccut}}$ . Typically the calculated diagonal  $\Delta V_{ii}^{\text{xc}}(\mathbf{k})$  is reasonably linear in energy in the window 2 – 4 Ry above  $E_{\text{F}}$ , and the approximation is a reasonable one. In any case the contribution from these high-lying states affect QPE’s in the range of interest ( $E_{\text{F}} \pm 1$  Ry) very slightly; they depend minimally on what diagonal matrix is taken. Even neglect of the diagonal part altogether ( $a = 0$  and  $b = 0$ ) only modestly affects results ( $< 0.1$  eV change). We finally confirm the stability of the final results by monitoring how QPE’s depend on  $E_{\text{xccut}}$ . Generally the dependence of QPE’s on  $E_{\text{xccut}}$  for  $E_{\text{xccut}} > 2$  Ry is very weak.

The construction of the Hamiltonian then proceeds as follows:

$$\begin{aligned}
& \text{Make } \Delta V^{\text{xc}}, \text{ diagonalize } H^{\text{LDA}} \text{ in orbital basis:} \\
\Delta V_{\mathbf{R}'L'j',\mathbf{R}+\mathbf{T}Lj}^{\text{xc}} & \rightarrow \Delta V_{\mathbf{R}'L'j',\mathbf{R}Lj}^{\text{xc}}(\mathbf{k}) \\
H_{\mathbf{R}'L'j',\mathbf{R}+\mathbf{T}Lj}^{\text{LDA}} & \rightarrow \{z_{\mathbf{R}Lj,n}^{\mathbf{k},\text{LDA}}, \varepsilon_{\mathbf{k}n}^{\text{LDA}}\} \\
& \text{Rotate } \Delta V^{\text{xc}} \text{ to LDA basis; patch high-energy parts:} \\
\Delta V_{\mathbf{R}'L'j',\mathbf{R}Lj}^{\text{xc}}(\mathbf{k}) & \rightarrow \begin{cases} \Delta V_{\tilde{n}\tilde{m}}^{\text{xc}}(\mathbf{k}), & \varepsilon_{\mathbf{k}\tilde{n}}^{\text{LDA}}, \varepsilon_{\mathbf{k}\tilde{m}}^{\text{LDA}} < E_{\text{xccut}} \\ (a\varepsilon_{\mathbf{k}\tilde{n}}^{\text{LDA}} + b)\delta_{\tilde{n}\tilde{m}} & \text{otherwise} \end{cases}
\end{aligned}$$

The Hamiltonian is then, in the LDA basis:  $H_{\tilde{n}\tilde{m}}(\mathbf{k}) = \varepsilon_{\mathbf{k}\tilde{n}}^{\text{LDA}}\delta_{\tilde{n}\tilde{m}} + \Delta V_{\tilde{n}\tilde{m}}^{\text{xc}}(\mathbf{k})$ .

In principle our results do not depend on the LDA. However, in our implementation we do not strictly eliminate the LDA potential. It is computationally convenient to use it as a framework around which the QSGW potential is added. As a result there remain small dependences on the LDA:

- (i) The MTO's are not fixed; the shape of the augmented functions ( $\varphi_{Rl}$ ,  $\dot{\varphi}_{Rl}$ ,  $\varphi_{Rl}^z$ ) depend on the generating potential, as do the core wave functions. We use the LDA as the generating potential.
- (ii) The replacement of the high-energy parts of  $\Delta V_{ii}^{\text{xc}}(\mathbf{k})$  by a diagonal part depends on the LDA, as noted above.
- (iii) When the spin-orbit coupling is included, it is computed perturbatively with the LDA potential:  $H_{\tilde{n}\tilde{m}}^0(\mathbf{k}) = H_{\tilde{n}\tilde{m}}^{\text{LDA}}(\mathbf{k}) + H_{\tilde{n}\tilde{m}}^{\text{SO,LDA}}(\mathbf{k}) + \Delta V_{\tilde{n}\tilde{m}}^{\text{xc}}(\mathbf{k})$ . Typically, the QSGW self-energy is made without SO coupling, and  $L \cdot S$  is included for a fixed  $V^{\text{xc}}$ . We can include the  $L_z S_z$ -only part of  $L \cdot S$  in the QSGW self-consistency cycle, though usually this is not necessary.

While all of these dependences on the LDA can be eliminated in principle, we do not expect any of them to significantly affect the final result. Point (i) makes little difference;  $sp$  partial waves functions are little changed, and we use local orbitals for  $d$  and  $f$  waves to ensure the basis is complete. (It is possible that some effect would result from changing the shape of the core wave functions.) As regards point (ii), QPE's are depend very weakly on high-lying parts of  $\Delta V_{nm}^{\text{xc}}(\mathbf{k})$ ; whether the cutoff is made in an LDA basis or an QSGW basis is of negligible importance. Finally, it is possible that spin-orbit coupling computed by an QSGW potential would differ somewhat from the LDA potential.  $H^{\text{SO}}$  depends on the radial derivative  $\partial V/\partial r$ . It is dominant for relatively small  $r$  where  $V$  is rapidly changing, and we do not expect it matters a great deal whether the LDA or QSGW potential is used. In any case  $H^{\text{SO}}$  is small.

### III. NUMERICAL RESULTS

Here, we first show some convergence tests, and then show results for some kinds of materials to explain how QSGW works.

#### A. Convergence Test for Mixed basis

Table I shows convergence checks of the mixed basis (product basis and IPW's) expansion of  $W$ , and the convergence in IPW's for eigenfunctions. We take GaAs, where we use 92 MTO basis set for valence:

Ga:  $4s \times 2 + 4p \times 2 + 3d \times 2 + 4f + 5g + 4d(\text{local})$ ; 39 functions ;

As:  $4s \times 2 + 4p \times 2 + 3d \times 2 + 4f + 5g + 5s(\text{local})$ ; 35 functions;

Fl:  $1s + 2p + 3d$ ; 18 functions.

"FI" denotes floating orbitals (MTO's with zero augmentation radius [9]) centered at the two interstitial sites.

$H^0$  was made self-consistent for a reference case; then one-shot calculations were performed systematically varying parameters in the mixed basis. The result is shown in Table I, where computational cases are specified by the two numbers (or labels "Small" and "Big") in the left-end column. These are IPW cutoffs  $|\mathbf{q} + \mathbf{G}|_{\text{Max}}^{\Psi}$  and  $|\mathbf{q} + \mathbf{G}|_{\text{Max}}^W$  introduced in Sec. II C. The reference case is denoted by 3.5,2.6 meaning  $|\mathbf{q} + \mathbf{G}|_{\text{Max}}^{\Psi} = 3.6$  and  $|\mathbf{q} + \mathbf{G}|_{\text{Max}}^W = 2.6$ .

In the test (i) in Table I, we show the convergence with respect to  $|\mathbf{q} + \mathbf{G}|_{\text{Max}}^W$ .  $|\mathbf{q} + \mathbf{G}|_{\text{Max}}^W = 2.6 a.u.$  is sufficient for  $<0.01\text{eV}$  numerical convergence. Test (ii) is for  $|\mathbf{q} + \mathbf{G}|_{\text{Max}}^{\Psi}$ ; this also shows that 3.6 a.u. (even 3.0 a.u.) is sufficient  $<0.01\text{eV}$  convergence.

We can characterize the product basis by the number of radial functions in each  $l$  channel. In the reference case this consists of (5,5,6,4,3) and (6,6,6,4,2) functions for  $l_p = 0, \dots, 4$  on the Ga and As sites, respectively ( $l_p^{\text{MAX}} = 4$  in this case). The total number of functions is then  $5 \times 1 + 5 \times 3 + 6 \times 5 + 4 \times 7 + 3 \times 9 = 100$  on Ga, and 100 on As. The "Big" product basis of Table I used  $l_p^{\text{MAX}} = 5$  with (8,8,8,6,3,2) functions for  $l_p=0, \dots, 5$  on Ga and As (326 functions total), while the "Small" product basis had  $l_p^{\text{MAX}} = 2$  with (5,5,6) and (6,6,6) functions for  $l_p = 0, 1, 2$  on Ga and As. Test (iii) shows that the

GaAs	$\Gamma_{1c}$	$\Gamma_{15c}$	$X_{5v}$	$X_{1c}$	$X_{3c}$	$L_{3v}$	$L_{1c}$	$L_{3c}$
(i) varying $ \mathbf{q} + \mathbf{G} _{\text{Max}}^W$								
3.5,1.8	1.932	4.761	-2.973	2.026	2.452	-1.259	2.087	5.588
3.5,2.5	2.041	4.799	-2.935	2.168	2.566	-1.245	2.189	5.652
3.5,2.6	2.046	4.803	-2.933	2.175	2.571	-1.244	2.194	5.657
3.5,3.0	2.053	4.809	-2.930	2.186	2.580	-1.243	2.201	5.664
3.5,3.5	2.053	4.810	-2.929	2.188	2.581	-1.243	2.202	5.666
(ii) varying $ \mathbf{q} + \mathbf{G} _{\text{Max}}^V$								
2.6,2.6	2.038	4.795	-2.939	2.158	2.558	-1.247	2.183	5.647
3.0,2.6	2.045	4.801	-2.935	2.172	2.569	-1.245	2.192	5.654
3.5,2.6	2.046	4.803	-2.933	2.175	2.571	-1.244	2.194	5.657
(iii) varying the product basis for $W$								
Small	1.249	4.611	-3.202	1.702	2.133	-1.364	1.623	5.452
3.5,2.6	2.046	4.803	-2.933	2.175	2.571	-1.244	2.194	5.657
Big	2.057	4.811	-2.928	2.193	2.588	-1.243	2.207	5.669

TABLE I: Three tests for GaAs, showing convergence with respect to the number of the interstitial plane waves (IPW), and product basis. Calculations are performed for a  $4 \times 4 \times 4$   $\mathbf{k}$ -mesh, Eq. (52) (Results are not  $k$ -converged, but the differences between rows will not change significantly.) QPE's are in eV, relative to the top of valence. For tests (i) and (ii), numbers in the first column are cutoffs in the  $\mathbf{G}$ -vectors for wave functions ( $|\mathbf{q} + \mathbf{G}|_{\text{Max}}^V$ ) and Coulomb interaction ( $|\mathbf{q} + \mathbf{G}|_{\text{Max}}^W$ ).  $|\mathbf{q} + \mathbf{G}| = (3.5, 3.0, 2.6, 2.5, 1.8)$  a.u. correspond to (229,137,89,65,27) IPWs at  $\mathbf{q} = 0$ . The starting  $H^0$  was generated by the 3.5,2.6 case and was not updated to perform the other tests. Test (iii) used the reference IPW cutoffs and varied the product basis, as described in the text.

reference product basis is satisfactory; it is a typical one for calculations. Comparison with ‘‘Small’’ case shows that  $l_p^{\text{MAX}} = 2$  is poor; in our experience,  $l_p^{\text{MAX}}$  must be twice larger than the maximum  $l$  basis function that has significant electron occupancy.

In addition we tested many possible kinds MTO basis sets, similar to the tests presented for Si in Ref. [9]. For GaAs, e.g., removing the  $5g$  orbitals from Ga and As reduces the minimum band gap by  $\sim 0.05$  eV; adding  $4f \times 1 + 5g \times 1$  for floating orbitals increases it by  $\sim 0.03$  eV. In general we have found that it is difficult to attain satisfactory numerical stability (convergence) to better than  $\sim 0.1$  eV (this is a conservative estimate; we probably reach  $\sim 0.05$  eV or less for a simple semiconductor such as GaAs). This means that the numerical accuracy is mainly controlled by the quality of the eigenfunctions input to the  $GW$  calculation, not by the cutoff parameters as tested here.

### B. Test of $k$ point convergence

$\mathbf{k}$ -point convergence in  $GW$  calculations is somewhat harder to attain than in LDA calculation. Fig. 3 shows the dependence of the direct and  $\Gamma_{25v} \rightarrow X_{1c}$  gaps on  $n_k$ , calculated by QSGW. Data are plotted as  $1/n_k^3$ , where  $n_k^3 = N_1 N_2 N_3$  is the number of mesh points in the BZ see Eq. (52). Data is essentially linear in  $1/n_k^3$ , as it is in one-shot calculations[9, 50]. The figure enables us to estimate the error owing to incomplete  $k$  convergence by extrapolation to  $1/n_k^3 \rightarrow 0$ .

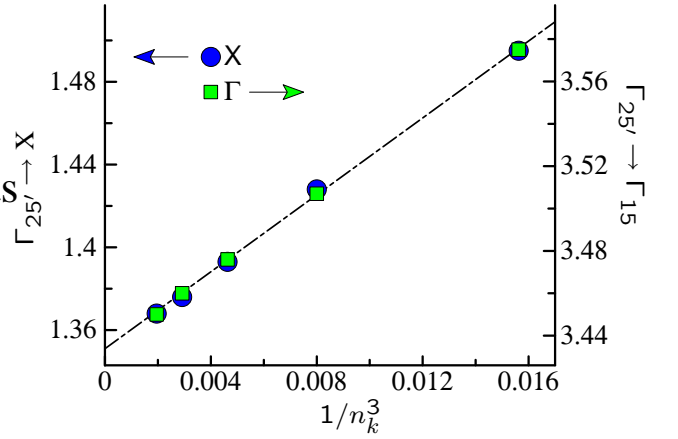


FIG. 3: Convergence in the  $\Gamma_{25'v} - X_{1c}$  (circles) and  $E_0 = \Gamma_{25'v} - \Gamma_{15c}$  (squares) gaps in Si with the density of  $k$  points in the Brillouin zone,  $1/n_k^3$ , calculated within the QSGW approximation. Points correspond to  $n_k = 4, 5, 6, 7, 8$ . Dot-dashed line is shown as a guide to the eye.

### C. C, Si, SiC, GaAs, ZnS and ZnSe

Table II-IV show QPE within various kinds of  $GWA$ , for C and Si, and for SiC, GaAs, ZnS and ZnSe in the zincblende structure. ‘1shot’ denotes the standard 1shot- $GW$  from the LDA including the  $Z$  factor, Eq. (7); we also show ‘1shotNZ’ starting from the LDA, but using Eq. (7) with  $Z=1$ . As noted by ourselves and others [6, 7, 8, 9, 38], standard ‘1shot’ generally underestimates band gaps relative to experiment; for example, the difference between ‘1shot,  $8 \times 8 \times 8$ ’ and LDA is  $0.97 - 0.46$  eV for bandgap of Si. This difference is only  $\sim 60\%$  of the

TABLE II: QPE relative to top of valence for various kinds of *GWA*, in eV. Calculations use  $6 \times 6 \times 6$  **k**-points, except rows labeled ‘ $8 \times 8 \times 8$ ’. *k* convergence can be estimated by comparing ‘mode-A’ and ‘mode-A, $8 \times 8 \times 8$ ’ (see also Fig. 3). ‘1shot’ denotes standard 1shot-*GW* with  $H^0 = H^{\text{LDA}}$ , Eq. (7). We also show ‘1shotNZ’ for the one-shot case with  $Z=1$ . ‘e-only’ denotes eigenvalue-only self-consistency: eigenvalues are updated but LDA eigenfunctions are retained. ‘mode-A’ corresponds to *QSGW* using Eq. (13), ‘mode-B’ to Eq. (14). ‘expt.+correction’ adds to the experimental value contributions from spin-orbit and zero-point motion (referred to as ‘Adj’ in Table III of Ref. [9]). Estimates for the latter are taken from Table III of Ref. [51]. Experimental data taken from compilations in Refs. [52] and [53] except where noted.

<b>C</b>	$\Gamma_{1v}$	$\Gamma_{15c}$	$\Gamma_{2'c}$	$X_{4v}$	$X_{1c}$	$L_{3'v}$	$L_{1c}$	$L_{3c}$	$E_g$
LDA	-21.32	5.55	13.55	-6.29	4.70	-2.79	9.00	8.39	4.09
1shot	-22.24	7.41	14.89	-6.69	6.07	-2.99	10.37	10.34	5.51
1shotNZ	-22.60	7.79	15.26	-6.80	6.33	-3.04	10.67	10.76	5.77
1shot, $8 \times 8 \times 8$	-22.25	7.38	14.87	-6.69	6.04	-2.99	10.35	10.32	5.48
1shotNZ, $8 \times 8 \times 8$	-22.62	7.76	15.23	-6.81	6.30	-3.05	10.64	10.73	5.74
e-only	-23.03	7.92	15.72	-6.92	6.53	-3.09	10.96	10.94	5.94
mode-A	-23.05	8.01	15.73	-6.89	6.54	-3.07	10.96	10.99	5.97
mode-A, $8 \times 8 \times 8$	-23.06	7.98	15.70	-6.90	6.52	-3.07	10.93	10.96	5.94
mode-B	-23.05	8.04	15.79	-6.89	6.55	-3.07	10.98	11.00	5.97
expt.	-23.0 <sup>a</sup>	7.14 <sup>b</sup>			6.08 <sup>c</sup>				5.5 <sup>c</sup>
expt.+correction					6.45 <sup>d</sup>				5.87 <sup>d</sup>

---

<b>Si</b>	$\Gamma_{1v}$	$\Gamma_{15c}$	$\Gamma_{2'c}$	$X_{4v}$	$X_{1c}$	$L_{3'v}$	$L_{1c}$	$L_{3c}$	$E_g$
LDA	-11.98	2.52	3.22	-2.86	0.59	-1.20	1.42	3.29	0.46
1shot	-11.90	3.14	4.04	-2.96	1.12	-1.25	2.07	3.91	0.98
1shotNZ	-11.90	3.34	4.30	-3.01	1.27	-1.28	2.26	4.11	1.13
1shot, $8 \times 8 \times 8$	-11.89	3.13	4.02	-2.96	1.11	-1.25	2.05	3.89	0.97 <sup>e</sup>
1shotNZ, $8 \times 8 \times 8$	-11.89	3.32	4.28	-3.01	1.25	-1.27	2.24	4.09	1.11
e-only	-12.17	3.36	4.30	-3.05	1.28	-1.29	2.26	4.14	1.14
mode-A	-12.20	3.47	4.40	-3.05	1.38	-1.28	2.36	4.25	1.25
mode-A, $8 \times 8 \times 8$	-12.19	3.45	4.38	-3.05	1.37	-1.28	2.35	4.23	1.23
mode-B	-12.21	3.52	4.49	-3.04	1.42	-1.28	2.42	4.29	1.28
expt.	-12.50	3.35 <sup>f</sup>	4.18	-2.9	1.32	-1.2	2.18 <sup>f</sup>	4.10 <sup>f</sup>	1.17
expt.+correction									1.24 <sup>g</sup>

<sup>b</sup>Ref. [54]

<sup>b</sup>Ref. [55]

<sup>c</sup>5.50 eV for fundamental gap on  $\Delta$  line [56], adding (calculated) difference 0.58 eV from  $\text{min} \rightarrow X$ .

<sup>d</sup>EP renormalization 0.37 eV [51]

<sup>e</sup>This number was 0.95 eV in Ref.[9] because of differences in computational conditions.

<sup>f</sup>Ellipsometry [57].  $L_c$  data assumes  $L_{3'v} = -1.28$  eV).

<sup>g</sup>Correction: 0.02 eV (SO) + 0.03 (EP renormalization) [51]

correction  $1.24 - 0.46$  eV needed for the calculation to be exact. The systematic tendency to underestimate gaps in ‘1shot’ is also confirmed by a recent FP-LAPW *GW* calculation [38] with huge basis sets. ‘1shotNZ’ shows better agreement with experiment; a justification for using  $Z=1$  was presented in Ref. [9]. However, this good agreement is somewhat fortuitous because of cancellation between two contributions to  $W$ : there is one contribution from the LDA bandgap underestimate, which overestimates  $\Pi$  and underestimates  $W$ , and another from omission of excitonic effects which overestimates  $W$  [9]. In other words, ‘1shot’ agreement with experiment would worsen if  $W$  were to include excitonic effects: the screening would be enhanced and result in smaller band gaps. ‘e-only’ denotes self-consistency in eigenvalues, while retaining LDA eigenfunctions (and charge density). ‘mode-A’ is *QSGW* with Eq. (13), ‘mode-B’ with Eq. (14). ‘mode-A, $8 \times 8 \times 8$ ’

is *k*-converged to  $\sim 0.01$  eV; see Fig. 3.

Tables II-IV shows that ‘e-only’ results are closer to ‘1shotNZ’ than ‘1shot’. We present results for a few materials here, but find that it appears to be true for a rather wide range of materials. We have already argued this point in Ref. [11]. Mahan compares the two in the context of the Frölich Hamiltonian [16]. The Rayleigh-Schrödinger perturbation theory corresponds to ‘1shotNZ’, which he argues is preferable to the Brillouin-Wigner perturbation which corresponds to ‘1shot’.

‘e-only’ and ‘mode-A’ do not differ greatly in these semiconductors, because the LDA eigenfunctions are similar to the *QSGW* eigenfunctions (this is evidenced by minimal differences in the LDA and *QSGW* charge densities). ‘mode-A’ band gaps are systematically larger than experiments, which we attribute to the omission of excitonic contributions to the dielectric function. ‘mode-A’

TABLE III: See caption for Table II.

SiC	$\Gamma_{1v}$	$\Gamma_{1c}$	$\Gamma_{15c}$	$X_{5v}$	$X_{1c}$	$L_{3v}$	$L_{1c}$	$L_{3c}$	
LDA	-15.31	6.25	7.18	-3.20	1.31	-1.06	5.38	7.13	
1shot	-15.79	7.18	8.54	-3.43	2.16	-1.14	6.51	8.41	
1shotNZ	-16.01	7.43	8.89	-3.51	2.36	-1.17	6.79	8.73	
1shot,8×8×8	-15.79	7.16	8.53	-3.43	2.14	-1.14	6.49	8.39	
1shotNZ,8×8×8	-16.01	7.42	8.87	-3.51	2.34	-1.17	6.77	8.71	
e-only	-16.33	7.71	9.09	-3.56	2.51	-1.18	6.99	8.95	
mode-A	-16.35	7.70	9.13	-3.58	2.53	-1.18	7.01	8.97	
mode-A,8×8×8	-16.35	7.69	9.12	-3.57	2.52	-1.18	7.00	8.96	
mode-B	-16.34	7.78	9.18	-3.58	2.58	-1.18	7.07	9.01	
expt. <sup>a</sup>					2.39				
GaAs	Ga 3d at $\Gamma$	$\Gamma_{1c}$	$\Gamma_{15c}$	$X_{5v}$	$X_{1c}$	$X_{3c}$	$L_{3v}$	$L_{1c}$	$L_{3c}$
LDA	-14.87, -14.79	0.34	3.67	-2.72	1.32	1.54	-1.16	0.86	4.58
1shot	-16.75, -16.70	1.44	4.30	-2.86	1.76	2.11	-1.22	1.66	5.14
1shotNZ	-17.64, -17.60	1.75	4.49	-2.91	1.88	2.26	-1.24	1.88	5.32
1shot,8×8×8	-16.75, -16.69	1.41	4.27	-2.86	1.74	2.08	-1.23	1.64	5.12
1shotNZ,8×8×8	-17.65, -17.61	1.70	4.46	-2.91	1.85	2.23	-1.25	1.85	5.29
e-only	-17.99, -17.97	1.69	4.58	-2.94	1.97	2.32	-1.26	1.89	5.44
mode-A	-18.13, -18.07	1.97	4.77	-2.93	2.15	2.54	-1.24	2.14	5.63
mode-A,8×8×8	-18.13, -18.07	1.93	4.74	-2.93	2.12	2.51	-1.25	2.11	5.60
mode-B	-18.10, -18.04	2.03	4.80	-2.94	2.17	2.56	-1.25	2.18	5.65
expt.	-18.8 <sup>c</sup>	1.52 <sup>e</sup>	4.51 <sup>e</sup>	-2.80 <sup>c</sup>	2.11 <sup>e</sup>		-1.30 <sup>c</sup>	1.78 <sup>e</sup>	
expt.+correction		1.69 <sup>f</sup>							

<sup>a</sup>Ref. [58]<sup>c</sup>Photoemission data, Ref. [59] (Ref. [60] for Ga 3d levels)<sup>e</sup>Ellipsometry from Ref. [61].  $L_c$  and  $X_c$  assume  $L_{4,5v} = -1.25$  eV,  $X_{7v} = -3.01$  eV (QSGW results with SO)<sup>f</sup>Corrections include 0.11 eV (SO) + 0.06 eV(EP)

and ‘mode-B’ show only slight differences, which is indicator of the ambiguity in the QSGW scheme due to the different possible choices for the off-diagonal contributions to  $V^{xc}$ . This shows the ambiguity is not so serious a problem in practice.

Fundamental gaps are precisely known; other highly indirect gaps are well known only in a few materials. Much better studied are direct transitions from measurements seen as critical points in the dielectric function or reflectivity measurements. We present some experimental data for higher-lying states at  $\Gamma$ , and also X and L assuming QSGW values for the valence bands states from which the transitions are measured. Agreement is generally very systematic:  $\Gamma$ - $\Gamma$  and  $\Gamma$ -L transitions are usually overestimated by  $\sim 0.2$  eV, and  $\Gamma$ -X transitions a by little less. We can expect valence band dispersions to be quite reliable in QSGW; they are already reasonably good at the LDA level. Except for a handful of cases (GaAs, Si, Ge, and certain levels in other semiconductors) there remains a significant uncertainty in the QP levels other than the minimum gap. In ZnSe, for example, the L point was inferred to be 4.12 eV from a fast carrier dynamics measurement [66], while optical data show  $\sim 0.2$  eV variations in  $E_1 = L_{1c} - L_{3'v}$ ; compare, for example Refs.[67] and [65]. Most of the photoemission data (used for occupied states in Tables II-IV) is also only reliable to a precision of a few tenths of an eV.

Finally, when comparing to experiment, we must add corrections for spin-orbit coupling and electron-phonon (EP) renormalization of the gap owing to zero-point motion of the nuclei. Neither are included in the QP calculations, and both would reduce the QSGW gaps. EP renormalizations have been tabulated for a wide range of semiconductors in Ref. [51]. In some cases there appears to be some experimental uncertainty in how large it is. In Si for example, the EP renormalization was measured to be  $\sim 0.2$  eV in Ref.[68], while the studies of Cardona and coworkers put it much smaller[51].

#### D. ZnO and Cu<sub>2</sub>O

Data for the direct gap at  $\Gamma$  for wurzite ZnO, and for Cu<sub>2</sub>O (cuprite structure) are given in Table V. In these materials, ‘1shotNZ’ (and more so ‘1shot’) results are rather poor, as were ZnS and ZnSe (Table IV). Corresponding energy bands are shown in Figs. 4 and 6. We used 144 and 64  $\mathbf{k}$  points to make  $H^0$  for ZnO and Cu<sub>2</sub>O, respectively. ‘1shotNZ(off-d)’ denotes a 1shot calculation, including the off-diagonal elements of  $\Delta V^{xc}$  computed in ‘mode-A’; i.e. bands were generated by  $H^{LDA} + \Delta V^{xc}$  without self-consistency. They differ little from standard ‘1shotNZ’ results in semiconductors, as we showed for variety of materials in Ref. [9]. Calculated

TABLE IV: See caption for Table II.

$\beta$ -ZnS	$\Gamma_{1v}$	Zn 3d at $\Gamma$	$\Gamma_{1c}$	$\Gamma_{15c}$	$X_{5v}$	$X_{1c}$	$X_{3c}$	$L_{3v}$	$L_{1c}$	$L_{3c}$
LDA	-13.10	-6.44, -5.95	1.86	6.22	-2.23	3.20	3.89	-0.87	3.09	6.76
1shot	-12.92	-7.29, -6.93	3.23	7.73	-2.34	4.33	5.36	-0.92	4.58	8.20
1shotNZ	-12.92	-7.74, -7.42	3.59	8.15	-2.39	4.62	5.76	-0.94	4.97	8.61
1shot, $8 \times 8 \times 8$	-12.92	-7.29, -6.94	3.21	7.72	-2.35	4.32	5.35	-0.92	4.57	8.19
1shotNZ, $8 \times 8 \times 8$	-12.93	-7.75, -7.42	3.57	8.14	-2.39	4.61	5.74	-0.94	4.96	8.59
e-only	-13.52	-8.14, -7.82	3.83	8.47	-2.44	4.91	6.01	-0.96	5.22	8.95
mode-A	-13.50	-8.33, -7.97	4.06	8.69	-2.43	5.06	6.24	-0.95	5.47	9.14
mode-A, $8 \times 8 \times 8$	-13.50	-8.33, -7.97	4.04	8.68	-2.43	5.05	6.23	-0.95	5.45	9.13
mode-B	-13.53	-8.31, -7.94	4.13	8.75	-2.44	5.12	6.30	-0.95	5.53	9.20
expt.		-8.7 <sup>a</sup>	3.83 <sup>b</sup>							
expt.+correction			3.94 <sup>c</sup>							

---

ZnSe	$\Gamma_{1v}$	Zn3d at $\Gamma$	$\Gamma_{1c}$	$\Gamma_{15c}$	$X_{5v}$	$X_{1c}$	$X_{3c}$	$L_{3v}$	$L_{1c}$	$L_{3c}$
LDA	-13.32	-6.64, -6.27	1.05	5.71	-2.21	2.82	3.32	-0.88	2.36	6.30
1shot	-13.15	-7.66, -7.39	2.31	6.82	-2.35	3.62	4.41	-0.94	3.57	7.32
1shotNZ	-13.09	-8.17, -7.94	2.63	7.14	-2.40	3.82	4.70	-0.96	3.89	7.62
1shot, $8 \times 8 \times 8$	-13.16	-7.66, -7.39	2.28	6.80	-2.35	3.60	4.40	-0.94	3.56	7.31
1shotNZ, $8 \times 8 \times 8$	-13.10	-8.18, -7.94	2.59	7.12	-2.40	3.80	4.68	-0.96	3.86	7.60
e-only	-13.61	-8.52, -8.30	2.79	7.41	-2.43	4.08	4.92	-0.97	4.08	7.93
mode-A	-13.64	-8.63, -8.36	3.11	7.69	-2.42	4.32	5.20	-0.96	4.39	8.19
mode-A, $8 \times 8 \times 8$	-13.65	-8.63, -8.36	3.08	7.68	-2.42	4.30	5.19	-0.96	4.38	8.17
mode-B	-13.65	-8.65, -8.38	3.16	7.72	-2.42	4.34	5.23	-0.96	4.43	8.21
expt.		-9.0 <sup>d</sup>	2.82 <sup>e</sup>		-2.1 <sup>d</sup>	4.06 <sup>f</sup>		-1.2 <sup>d</sup>	3.96 <sup>f</sup>	
expt.+correction			3.00 <sup>g</sup>							

<sup>a</sup>Ref. [62]<sup>b</sup>Ref. [63]<sup>c</sup>Corrections include 0.02 eV (SO) + 0.09 eV(EP) [51]<sup>d</sup>Ref. [64]<sup>e</sup>Ref. [63]<sup>f</sup>Reflectivity from Ref. [65].  $L_c$  and  $X_c$  assume  $L_{4,5v}=-0.95$  eV,  $X_{7v}=-2.47$  eV (QSGW results with SO)<sup>g</sup>Corrections include 0.13 eV (SO) + 0.05 eV(EP) [51]TABLE V: Direct gap (eV) at  $\Gamma$  for ZnO and Cu<sub>2</sub>O for kinds of GWA. For Cu<sub>2</sub>O,  $E_g$  and  $E_0$  are the first and second minimum gap at  $\Gamma$ .

Material	Expt. +corr	LDA	1shot	1shotNZ	1shotNZ (off-d)	e-only	mode-A
ZnO	3.60 <sup>q</sup>	0.71	2.46	2.88	3.00	3.64	3.87
Cu <sub>2</sub> O $E_g$	2.20 <sup>q</sup>	0.53	1.51	1.99	1.95	1.98	2.36
$E_0$	2.58 <sup>q</sup>	1.29	1.88	1.97	1.93	2.32	2.81

<sup>q</sup>Values computed from 3.44+0.164 eV, 2.17+0.033 eV, and 2.55+0.033 eV, where 0.164eV and 0.033eV are zero-point contributions; See Table III in Ref. [51]. The 1shot value 2.46 eV for ZnO is slightly different from a prior calculation (2.44 eV in Ref. [37]) because of more precise computational conditions. ‘1shotNZ(off-d)’ denotes a 1shot calculation including the off-diagonal elements.

TABLE VI: Optical dielectric constant  $\epsilon_\infty$  calculated in the RPA[69] from ‘mode-A’  $H^0$ . Calculations were checked for  $k$ -convergence; data shown used 3888  $k$ -points for ZnO and 1444 points for the others. ‘With LFC’ means including the local field correction (See e.g.[15]).

	no LFC	with LFC	Expt.
ZnO( $k//C$ -axis)	3.2	3.0	3.75-4.0 <sup>a</sup>
Cu <sub>2</sub> O	5.9	5.5	6.46 <sup>b</sup>
MnO	3.9	3.8	4.95 <sup>c</sup>
NiO	4.4	4.3	5.43, 5.7 <sup>c</sup>

<sup>a</sup>Ref. [52]<sup>b</sup>Ref. [70]<sup>c</sup>Ref. [71, 72]<sup>d</sup>Ref. [73]

### 1. ZnO

dielectric constants  $\epsilon_\infty$  are shown in Table VI. Note its systematic underestimation. ‘With LFC’ is better theoretical estimate including the so-called local field correction (See e.g.[15]).

In contract to cases in previous section, ‘e-only’ and ‘1shotNZ’ now show sizable differences. This is because the LDA gap is much too small, and  $W$  is significantly overestimated. The discrepancy is large enough that ‘1shotNZ,’ which approximately corresponds to ‘e-only’

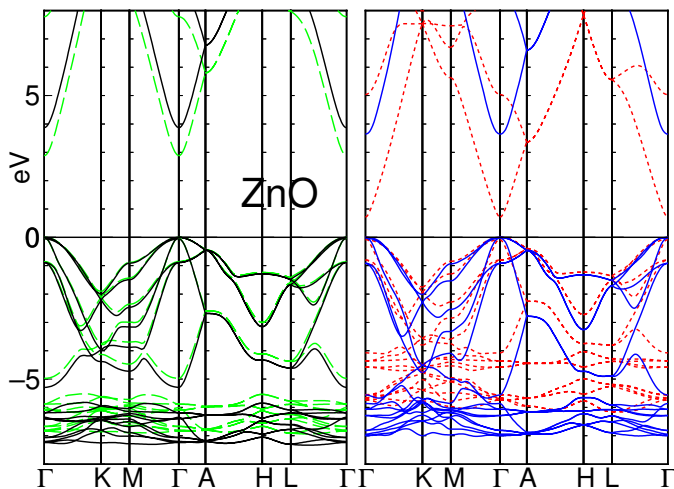


FIG. 4: Energy bands in wurzite ZnO. Solid(Black) in left panel:QSGW(‘mode-A’); Broken(Green) in left:1shotNZ(off-d); Solid(Blue) in right panel:‘e-only’; Dotted(Red) in right panel:LDA.

but neglecting changes in  $W^{\text{LDA}}$ , is no longer a reasonable approximation. On the other hand, Table V shows that the ‘e-only’ and ‘mode-A’ are not so different (3.64 eV compared to 3.87 eV). This difference measures the contribution of the off-diagonal part to band gap; it is similar to ZnS. This modest difference suggests that the LDA eigenfunctions are still reasonable. However, there still remains a difficulty in disentangling  $d$  valence bands from the others in the ‘e-only’ case: topological connections in band dispersions can not be changed from the LDA topology, as we discussed in Ref. [9].

The imaginary part of the dielectric function,  $\text{Im } \epsilon(\mathbf{q}=0, \omega)$ , is calculated from the ‘mode-A’ potential and compared to the experimental function in Fig. 5. There is some discrepancy with experiment. Arnaud and Alouani [15] calculated the excitonic contribution to  $\text{Im } \epsilon(\omega)$  with the Bethe-Salpeter equation for several semiconductors. Generally speaking, such a contribution can pull down peaks in  $\text{Im } \epsilon(\mathbf{q}=0, \omega)$  to lower energy and make peak structures just around the band edge. It is in fact just what is needed to correct the discrepancy with experiments as seen in Fig. 5. Similarly we expect that electron-hole interactions (excitonic effects) will largely correct the discrepancy between the QSGW  $\text{Im } \epsilon(\mathbf{q}=0, \omega)$  and experiment (see also  $\text{Cu}_2\text{O}$  below).

## 2. $\text{Cu}_2\text{O}$

We have to distinguish between the QP density of states (QP-DOS), which is calculated from  $H^0$  (the poles of  $G^0$ ), and the ‘spectrum’ density-of-states, which is calculated from the poles of  $G$ . The QP-DOS is the important quantity needed to describe the fundamental excitations in materials. QP-DOS in ‘mode-A’ are shown

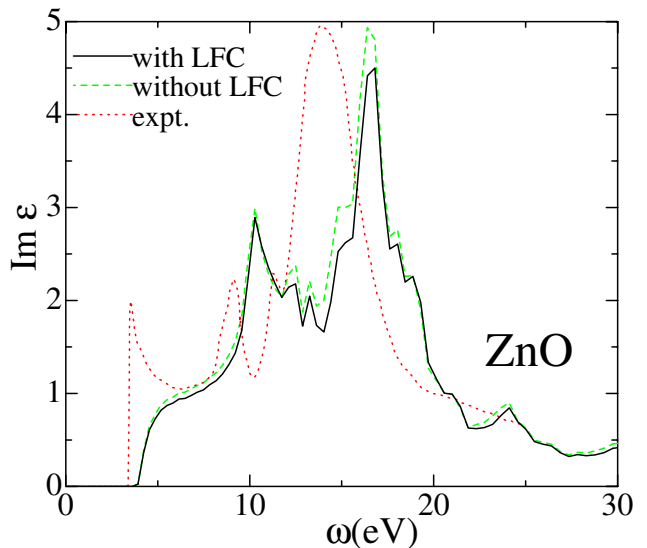


FIG. 5: Imaginary part of dielectric function for ZnO. Local field corrections (LFC) only slightly affect the result.

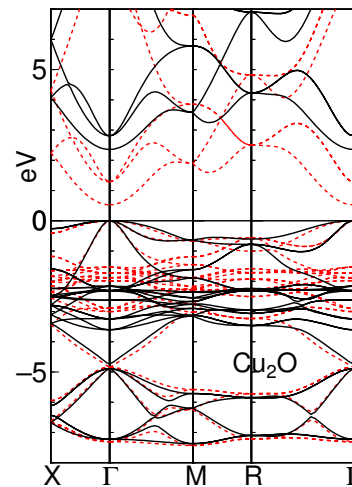


FIG. 6: Energy bands of  $\text{Cu}_2\text{O}$ . Dotted(Red):LDA ; Solid(Black):QSGW(‘mode-A’).

in Figs. 7. The absorption coefficient in RPA from  $H^0$  is shown in Fig. 8, as well as the energy bands in Fig. 6. This calculation includes  $\text{Cu}3p$  and  $\text{Cu}4d$  as VAL states using local orbitals.

As shown in Table V, the discrepancy between ‘e-only’ and ‘mode-A’ fundamental gap is  $\sim 0.4$  eV, rather significant and larger than cases considered previously. This reflects an increased discrepancy between the LDA and QSGW eigenfunctions. The ‘mode-A’ energy bands can be compared with results by Bruneval et al. [75], who also performed QSGW calculations within a pseudopotential framework. The lowest and second gaps we obtain,  $E_g=2.36$  eV and  $E_0=2.81$  eV, are somewhat larger than their values (1.97 eV and 2.27 eV). Further, the difference between the peaks just below  $E_{\text{Fermi}}$  and the

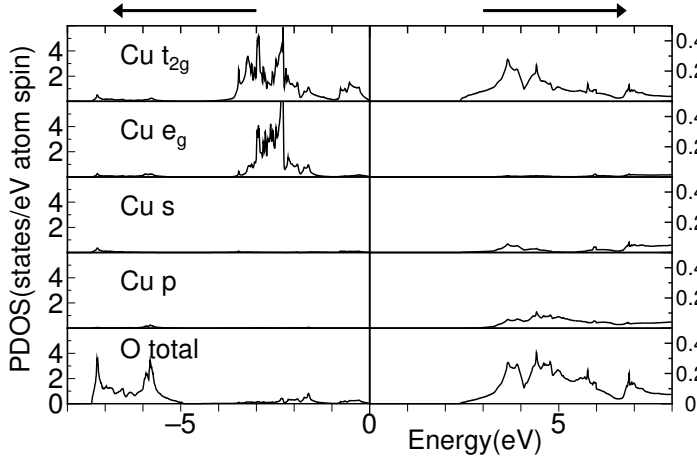


FIG. 7: Partial DOS (QP-DOS) computed from the QSGW  $H^0$  for  $\text{Cu}_2\text{O}$ . Valence band maximum at zero. Right-hand scale is for unoccupied states and is  $10\times$  the left-hand scale, which applies to occupied states.

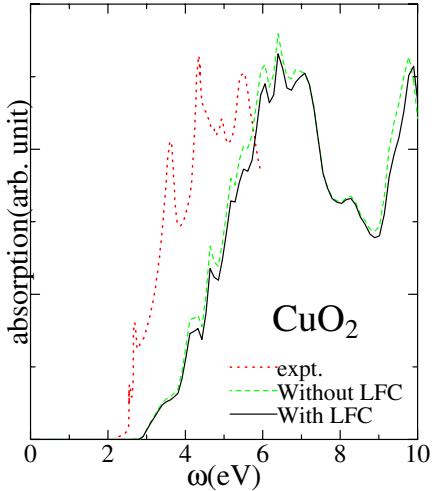


FIG. 8: Absorption coefficient for  $\text{Cu}_2\text{O}$ . Experiment is taken from Ref. [74].

main  $3d$  peak is 1.90 eV, which is slightly larger than what Bruneval et al. obtain (1.64 eV). This is the D1-F1 difference in Ref. [76], measured to be 1.94 eV. The absorption coefficient shows essentially the same kinds of discrepancy with experiment as we saw for  $\text{Im}\epsilon(\omega)$  in ZnO. Bruneval et al. calculated the excitonic contributions for  $\text{Cu}_2\text{O}$  in a Bethe-Salpeter framework [75], and showed that they account for most of the error in the RPA dielectric function as computed by QSGW.

### E. NiO and MnO

We described these compounds already in Ref. [10]; here we present some additional analysis. We assume antiferro-II ordering [77] and time-reversal symmetry

(thus no orbital moments), with 64  $\mathbf{k}$ -points in the BZ. In Fig. 9, we show QSGW ‘mode-A’ energy bands, comparing them to ‘e-only’ and LDA in the right panel. The problem with ‘e-only’ bands is now very apparent: the bandgap is much too small and the conduction band dispersions are qualitatively wrong (minimum gap falls at the wrong point for NiO). Further, the valence bands (especially, the relative position of O  $2p$  and TM  $3d$  bands) changes little relative to the LDA. ‘e-only’ can not change the LDA’s spin moment since eigenfunctions do not change; they are significantly underestimated. The QP-DOS are shown in Fig. 10.

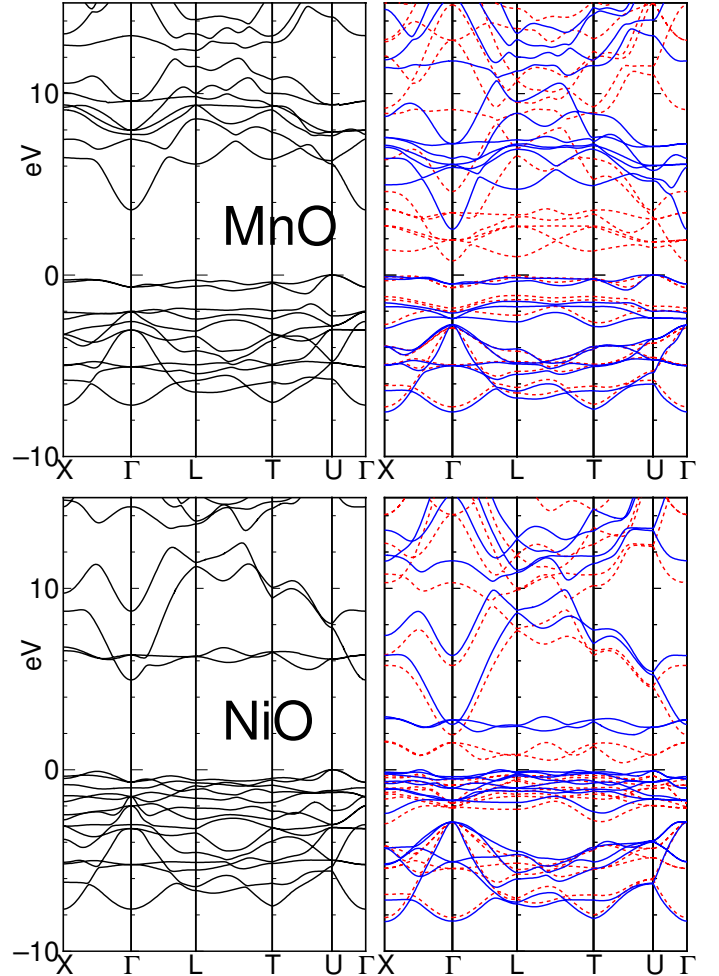


FIG. 9: Energy bands for NiO and MnO. Solid(Black) in left panel: QSGW(‘mode-A’) ; Solid(Blue) in right panel: ‘e-only’ ; Dotted(Red) in right panel: LDA.

#### 1. MnO

The Mn  $e_g$  and O  $2p$  QP-DOS show common peaks below  $E_{\text{Fermi}}$ . This is because of the strong  $dd_\sigma$  coupling between  $e_g$ , mediated through the O  $2p$  valence bands [77]. The  $e_g$  components are separated mainly into two peaks

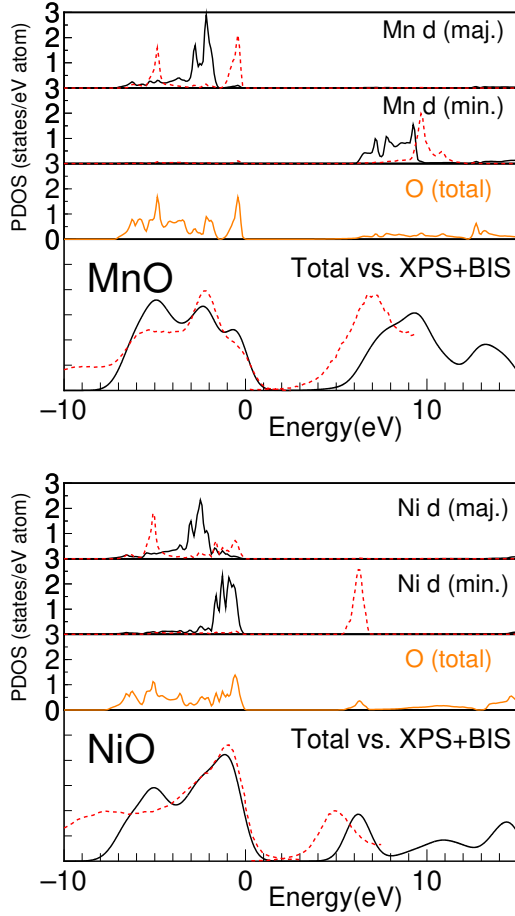


FIG. 10: QP-DOS(‘mode-A’) for NiO and MnO for each atomic site. Contributions are decomposed majority and minority in Mn(Ni) site in top two panels. Further, it is decomposed into  $e_g$  and  $t_{2g}$ . Dotted(Red):  $e_g$ ; Solid(Black):  $t_{2g}$ . O(total) is the QP-DOS project onto an O site (sum of majority and minority). Dots(Red) in the bottom panels are taken from XPS+BIS experiments [78, 79], and are compared with total QP-DOS broadened with a 0.6 eV Gaussian.

which have comparable weight, in contradiction to the LDA case where the deeper peak has a very small weight. This is because  $e_g$  levels are pushed down relative to the LDA. The bottom panel compares XPS (occupied states) and BIS (unoccupied states) experiments with the total QP-DOS, broadened with 0.6 eV Gaussian. There is good agreement with the XPS part for the  $e_g$  peak just below  $E_{\text{Fermi}}$ , for the  $t_{2g}$  peak, and for the valence band width. (Based on a model analysis by Takahashi and Igarashi [81], we expect that many-body effects do not strongly perturb the QP-DOS: that is the QP-DOS density of states will be similar to that calculated from the imaginary part of  $G$ .) However, there is discrepancy in the BIS part. A possible assignment is to identify a shoulder of total QP-DOS seen at  $\sim E_{\text{Fermi}}+7\text{eV}$  as the peak of the BIS at  $\sim 6.8\text{eV}$  (as claimed in Ref. [10]). Alternatively it is possible that the QP-DOS predicts conduction

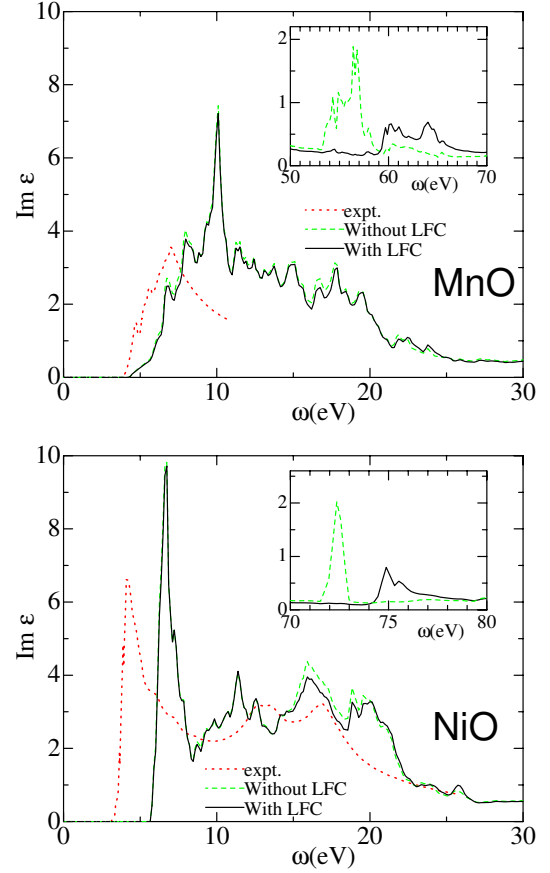


FIG. 11: Imaginary part of the dielectric function in MnO and NiO. Effects of local fields (LFC) are significant only in the deep energy region related to the  $3p$  core. It can be interpreted in terms of Lorenz’s field treatment as in the derivation of the Clausius-Mossotti’s relation. Expt. data is taken from Ref. [80] for MnO, and Ref. [73] for NiO.

bands  $\sim 1.5\text{eV}$  higher than the BIS data.

Fig. 11 compares  $\text{Im}\epsilon(\omega)$  generated by QSGW ‘mode-A’ with experiment. The discrepancy looks too large to explain the difference between the ‘mode-A’ calculation and the experimental data. However, if we neglect the difference in absolute value, we can say that ‘mode-A’ predicts the peak  $\text{Im}\epsilon(\omega)$  at an energy too high by  $\sim 2\text{eV}$ . This view is consistent with the conjecture below for NiO.

## 2. NiO

The majority-spin QP-DOS of NiO is roughly similar to that of MnO. However, the  $e_g$  state just below  $E_{\text{Fermi}}$  is broadened and carries less weight (Fig. 10). That peak is seen in MnO but is lost in this case, though the deeper  $e_g$  peak remains. The  $t_{2g}$  DOS is widened relative to LDA. These features are also observed in other beyond-LDA calculations [82, 83]. The top of valence consists of O  $2p$  states, which hybridize with majority  $e_g$  states, and minority  $t_{2g}$  which weakly hybridize. In the bottom

panel, the  $d$  DOS between  $E_{\text{Fermi}}$  and  $E_{\text{Fermi}}-4\text{eV}$  falls in good agreement with XPS; but the valence DOS width differs from XPS, in contradistinction to MnO. The reason can be attributed to the satellite structure contained in the XPS data: e.g. Takahashi et al.[81] predict that a satellite should appear around  $E_{\text{Fermi}}-9\text{eV}$ .

Turning to the unoccupied states, we can see ‘mode-A’ puts a peak  $\sim 1.3\text{ eV}$  too high compared BIS peak at  $\sim E_{\text{Fermi}}+5\text{eV}$ . On the other hand,  $\text{Im}\epsilon(\omega)$  is in rather reasonable agreement with experiment except for a shift in the first peak by  $\sim 2.0\text{ eV}$  (‘mode-A’). Thus we can distinguish two kinds errors in bandgap: (1.3 eV in BIS, and 2.0 eV in  $\text{Im}\epsilon$ ). We think both kinds of errors can be explained by the excitonic effects for  $W$  missing in our QSGW calculation. This is consistent with the QSGW  $\epsilon_{\infty}$  being underestimated. Thus our conjecture is: if we properly include the excitonic contributions to  $W$ , weights in  $\text{Im}\epsilon$  will shift to lower energy, resulting the higher  $\epsilon_{\infty}$ . Self-consistency with such  $W$  should reduce the band gap, resulting satisfactory agreement with both BIS and the dielectric function.

## F. Fe and Ni

Fig. 12 shows energy bands for Fe and Ni calculated by LDA, QSGW ‘mode-A’ and ‘e-only’. The two QSGW calculations show similar  $d$  band shapes: their widths narrow relative to LDA, moving into closer agreement with experiment. On the other hand, the ‘e-only’ calculation significantly shifts the relative positions of the  $s$  and  $d$  levels, depressing the bottom of  $s$  band  $\sim 1\text{ eV}$  in contradiction to experiment. ‘1shotNZ’ results (not shown) are very similar to the ‘e-only’ case. This indicates the importance of the charge redistribution due to the off-diagonal part of Eq. (13) in the  $3d$  transition metals. Yamasaki and Fujiwara [44] presented the ‘1shot’ GWA results for Fe, Ni, and Cu, Aryasetiawan [84] for Ni. Both calculations included the  $Z$  factor ( $Z \approx 0.8$  for  $s$  band,  $Z \approx 0.6$  for  $d$  band) thus the changes they found relative to LDA are not so large. Including the  $Z$  factor mostly eliminates the unwanted  $s$  band shift. However it does so apparently fortuitously. As ‘1shot’ (and ‘1shotNZ’) should be taken as an approximation of ‘e-only’, it is wrong to take ‘1shot’ as a better theoretical prediction than ‘e-only’.

## IV. SUMMARY

We showed that the QSGW formalism can be derived from a standpoint of self-consistent perturbation theory, where the unperturbed Hamiltonian is an optimized non-interacting one. Then we presented a means to calculate the total energy based on adiabatic connection, and how it relates to the density functional framework.

We then showed a number of key points in the implementation of our all-electron GWA and QSGW. The

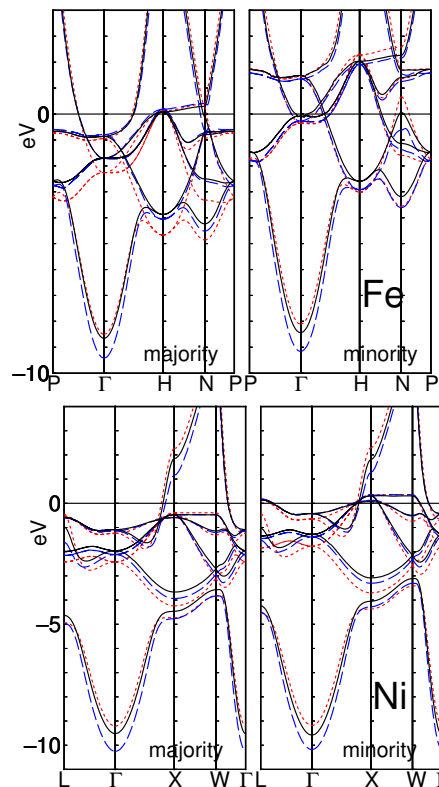


FIG. 12: Energy bands for Fe and Ni. Solid(Black): QSGW(‘mode-A’); Broken(Blue): ‘e-only’; Dotted(red): LDA. Calculations used  $12 \times 12 \times 12 = 1728$   $\mathbf{k}$ -points. Comparing to calculations at other  $\mathbf{k}$  meshes  $8 \times 8 \times 8 \dots 14 \times 14 \times 14$ , we estimate the numerical convergence is a little better than 0.1 eV. In this case convergence is limited by uncertainties in the determination  $E_{\text{Fermi}}$ [49]. Inspection of the bands at fine resolution show slight discontinuities at certain  $\mathbf{k}$  points. These occur at times because of difficulties in the  $\Sigma$  interpolation; see Sec. II G and the smearing procedure in Sec. II E.

mixed basis for  $W$  and the offset- $\Gamma$  method are especially important technical points. We presented some convergence checks for the mixed basis, and some results in various kinds of systems to demonstrate how well QSGW works. For insulators, QSGW provides rather satisfactory description of valence bands; conduction bands are also well described though bandgaps are systematically overestimated slightly. We compared the difference of the QSGW results to eigenvalue-only self-consistent results and to 1shot-GW results in various cases.

How well eigenvalue-only self-consistency works depends on how correlated the system is. In covalent semiconductors LDA eigenfunctions are rather good, and there is little difference. The error is no longer small in  $\text{Cu}_2\text{O}$ , Fe, and Ni; finally eigenvalue-only self-consistency fails qualitatively in NiO.

We would like to thank F. Aryasetiawan for giving us his LMTO-ASA GW code, which formed the basis for development of the present one. This work was supported by the DARPA SPINS project, and by ONR contract

N00014-02-1-1025.

- 
- [1] M. S. Hybertsen and S. G. Louie, Phys. Rev. B **34**, 5390 (1986).
- [2] L. Hedin, Phys. Rev. **139**, A796 (1965).
- [3] P. Hohenberg and W. Kohn, Phys. Rev. **136**, B864 (1964).
- [4] W. Kohn and L. J. Sham, Phys. Rev. **140**, A1133 (1965).
- [5] F. Aryasetiawan and O. Gunnarsson, Rep. Prog. Phys **61**, 237 (1998).
- [6] T. Kotani and M. van Schilfgaarde, Sol. State Commun. **121**, 461 (2002).
- [7] M. Usuda, H. Hamada, K. Siraishi, and A. Oshiyama, Jpn. J. Appl. Phys. Lett. (part 2) **43**, L407 (2004).
- [8] A. Fleszar and W. Hanke, Phys. Rev. B **71**, 045207 (2005).
- [9] M. van Schilfgaarde, T. Kotani, and S. V. Faleev (2006), in press, Phys. Rev. B. Preprint <http://arxiv.org/abs/cond-mat/0508295>.
- [10] S. V. Faleev, M. van Schilfgaarde, and T. Kotani, Phys. Rev. Lett. **93**, 126406 (2004).
- [11] M. van Schilfgaarde, T. Kotani, and S. Faleev, Phys. Rev. Lett. **96**, 226402 (pages 4) (2006), URL <http://link.aps.org/abstract/PRL/v96/e226402>.
- [12] A. N. Chantis, M. van Schilfgaarde, and T. Kotani, Phys. Rev. Lett. **96**, 086405 (2006), URL <http://link.aps.org/abstract/PRL/v96/e086405>.
- [13] A. N. Chantis, M. van Schilfgaarde, and T. Kotani (2006), submitted.
- [14] M. Alouani and J. M. Wills, Phys. Rev. B **54**, 2480 (1996).
- [15] B. Arnaud and M. Alouani, Phys. Rev. B **63**, 085208 (2001).
- [16] G. D. Mahan, *Many-Particle Physics* (Plenum Press, New York, 1990).
- [17] D. Pines and P. Nozieres, *The Theory of Quantum Liquid. Vol I* (W.A.Benjamin Inc., New York, 1966).
- [18] M. V. Fischetti and S. E. Laux, Phys. Rev. B **38**, 9721 (1988).
- [19] W.-D. Schöne and A. Eguiluz, Phys. Rev. Lett **81**, 1662 (1998).
- [20] W. Ku and A. G. Eguiluz, Phys. Rev. Lett. **89**, 126401 (2002).
- [21] G. Baym and L. P. Kadanoff, Phys. Rev. **124** (1961).
- [22] F. Bechstedt, K. Tenelsen, B. Adolph, and R. D. Sole, Phys. Rev. Lett. **78**, 1528 (1997).
- [23] Even starting from  $\Sigma[G]$  (the self-energy as a functional of  $G$ ), we can derive the so-called  $G^0W^0$  approximation (usual  $GWA$  based on  $G^0$  as in Sec.I.A). As  $G = Z \times G^0 +$  (incoherent part), we can pick up terms related to  $Z \times G^0$  in the expansion series with  $G$ . Then we can see that contributions from  $Z$  factors cancel out because of the Ward identity, which finally results in the  $G^0W^0$  approximation. Thus, if  $G^0W^0$  is good enough as we claim here,  $\Sigma[G]$  should be a very inefficient expansion, because there is too much cancellation between terms.
- [24] M. Springer, F. Aryasetiawan, and K. Karlsson, Phys. Rev. Lett. **80**, 2389 (1998).
- [25] S. Biermann, F. Aryasetiawan, and A. Georges, Phys. Rev. Lett. **90**, 086402 (2003).
- [26] M. Fuchs and X. Gonze, Phys. Rev. B **65**, 235109 (pages 4) (2002).
- [27] T. Miyake, F. Aryasetiawan, T. Kotani, M. van Schilfgaarde, M. Usuda, and K. Terakura, Phys. Rev. B **66**, 245103 (2002).
- [28] T. Kotani, J.Phys. Cond. Mat. **10** (1998).
- [29] R. Fukuda, T. Kotani, Y. Suzuki, and S. Yokojima, Progress of Theoretical Physics **92** (1994).
- [30] F. Aryasetiawan, T. Miyake, and K. Terakura, Phys. Rev. Lett. **88** (2002).
- [31] A. Marini, P. García-González, and A. Rubio, Phys. Rev. Lett. **96**, 136404 (2006).
- [32] R. Sakuma, S. Tsuneyuki, T. Kotani, and M. van Schilfgaarde, unpublished (2006).
- [33] A. Schindlmayr, Phys. Rev. B **56**, 3528 (1997).
- [34] A. Schindlmayr, P. Garcia, and R. W. Godby, Phys. Rev. B **64**, 235106 (2001).
- [35] M. Methfessel, M. van Schilfgaarde, and R. A. Casali, in *Lecture Notes in Physics*, edited by H. Dreyse (Springer-Verlag, Berlin, 2000), vol. 535.
- [36] E. Bott, M. Methfessel, W. Krabs, and P. C. Schmidt, J. Math. Phys. **39**, 3393 (1998).
- [37] M. Usuda, N. Hamada, T. Kotani, and M. van Schilfgaarde, Phys. Rev. B **66**, 125101 (2002).
- [38] C. Friedrich, A. Schindlmayr, S. Blügel, and T. Kotani, Phys. Rev. B **74**, 045104 (2006).
- [39] In the  $GW$  scheme as we have currently implemented it, CORE wave function can be obtained subject to the boundary condition that the value and slope vanish at the MT boundary. This procedure do not assure the orthogonality between CORE and VAL (the importance of orthogonality is seen at  $\mathbf{q} \rightarrow 0$  limit in dielectric function); this can be a source of error in the present treatment of CORE.
- [40] F. Aryasetiawan and O. Gunnarsson, Phys. Rev. B **49**, 16214 (1994).
- [41] J. Rath and A. Freeman, Phys. Rev. B **11**, 2109 (1975).
- [42] T. Miyake and F. Aryasetiawan, Phys. Rev. B **61**, 7172 (2000).
- [43] S. Lebègue, B. Arnaud, M. Alouani, and P. E. Bloechl, Phys. Rev. B **67**, 155208 (2003).
- [44] A. Yamasaki and T. Fujiwara, J. Phys. Soc. Japan **72**, 607 (2003).
- [45] F. Gygi and A. Baldereschi, Phys. Rev. B **34**, 4405 (1986).
- [46] R. W. Godby, M. Schlüter, and L. J. Sham, Phys. Rev. B **37**, 10159 (1988).
- [47] F. Aryasetiawan, *The GW approximation and vertex correction* (G & B Science Pub, 2000).
- [48] T. Kotani, J.Phys. Cond. Mat. **12** (2000).
- [49] There is some ambiguity in the metal case, about whether it is better to use the same mesh in both the “small loop” and the generation of  $\Sigma$ , or to use a finer mesh for a given  $\Delta V^{xc}(\mathbf{q})$ . The consistent mesh is preferable in that states above and below  $E_{\text{Fermi}}$  are counted in a consistent way; i.e. there is a consistency between  $\Sigma$  and  $V_{\text{H}}$ . Using a finer mesh for the small loop is preferable because the kinetic energy is a much more sensitive function of Fermi-surface

- effects than  $V^{\text{xc}}$ , which is determined by the small loop. Using a consistent mesh that is well converged in the kinetic energy can require unrealistically large numbers of  $\mathbf{k}$  points (something like  $16^3$  points in Fe for 0.01 eV accuracy). Usually the ambiguity is rather small on the scale of other uncertainties in the calculation.
- [50] N. Hamada, M. Hwang, and A. J. Freeman, Phys. Rev. B **41**, 3620 (1990), URL <http://link.aps.org/abstract/PRB/v41/p3620>.
- [51] M. Cardona and M. L. W. Thewalt, Rev. Mod. Phys. **77**, 1173 (2005).
- [52] S. Adachi, *Handbook On Physical Properties Of Semiconductors*, vol. 3 (Kluwer Academic, Boston, 2004).
- [53] O. Madelung, *Semiconductors Basic Data* (Springer-Verlag, Berlin, 1996).
- [54] I. Jiménez, L. J. Terminello, D. G. J. Sutherland, J. A. Carlisle, E. L. Shirley, and F. J. Himpsel, Phys. Rev. B **56**, 7215 (1997).
- [55] S. Logothetidis, J. Petalas, H. M. Polatoglou, and D. Fuchs, Phys. Rev. B **46**, 4483 (1992).
- [56] F. J. Himpsel, J. A. Knapp, J. A. VanVechten, and D. E. Eastman, Phys. Rev. B **20**, 624 (1979).
- [57] P. Lautenschlager, M. Garriga, L. Vina, and M. Cardona, Phys. Rev. B **36**, 4821 (1987).
- [58] *Crystal and Solid State Physics, Vol. 22A*, Landolt-Börnstein; *Numerical Data and Functional Relationships in Science and Technology* edited by O. Madelung (Springer, Berlin, 1984).
- [59] E. A. Kraut, R. W. Grant, J. R. Waldrop, and S. P. Kowalczyk, Phys. Rev. Lett. **44**, 1620 (1980).
- [60] L. Ley, R. A. Pollak, F. R. McFeely, S. P. Kowalczyk, and D. A. Shirley, Phys. Rev. B **9**, 600 (1974).
- [61] P. Lautenschlager, M. Garriga, S. Logothetidis, and M. Cardona, Phys. Rev. B **35**, 9174 (1987).
- [62] L. Zhou, T. A. Callcott, J. J. Jia, D. L. Ederer, and R. Perera, Phys. Rev. B **55**, 5051 (1997).
- [63] A. Mang, K. Reimann, S. Rübenacke, and M. Steube, Phys. Rev. B **53**, 16283 (1996).
- [64] C. J. Vesely, R. L. Hengehold, and D. W. Langer, Phys. Rev. B **5**, 2296 (1972).
- [65] R. Markowski, M. Piacenti, D. Debowska, M. Zinnal-Starnawska, F. Lama, N. Zema, and A. Kisiel, J. Phys.: Cond. Mat. **6**, 3207 (1994).
- [66] D. J. Dougherty, S. B. Fleischer, E. L. Warlick, J. L. House, G. S. Petrich, L. A. Kolodziejski, , and E. P. Ippen, Appl. Phys. Lett. **71**, 3144 (1997).
- [67] S. Adachi and T. Taguchi, Phys. Rev. B **43**, 9569 (1991).
- [68] H. Moriya, A. Kaneta, and S. Adachi, Mater. Sci. Eng. B **76**, 232 (2000).
- [69] Both numerator and denominator in the calculation of  $\Pi$  vanish as  $\mathbf{k} \rightarrow 0$  and  $\omega \rightarrow 0$ . Thus we need careful to carefully extrapolate to  $\mathbf{k} \rightarrow 0$  from  $\epsilon(\mathbf{k}, \omega = 0)$ . But we found that just using  $|\mathbf{k}| \sim 0.02 - 0.03$  a.u. is usually good sufficient to determine  $\epsilon$  to one-tenth of digit for these cases without any numerical difficulties.
- [70] J. W. Hodby, T. E. Jenkins, C. Schwab, H. Tamura, and D. Trivich, J. Phys. C: Solid State Phys. **9**, 1429 (1976).
- [71] S. Mochizuki, J. Phys.: Condens. Matter **1** (1989).
- [72] J. N. Plendl, L. C. Mansur, S. S. Mitra, and I. F. Chang, Solid State Communications **7**, 109 (1969).
- [73] R. J. Powell and W. E. Spicer, Phys. Rev. B **2**, 2182 (1970).
- [74] S. Brahms, S. Nikitine, and J. Dahl, Physics Letters **22**, 31 (1966).
- [75] F. Bruneval, N. Vast, L. Reining, M. Izquierdo, F. Sirotti, and N. Barrett (2006), submitted.
- [76] Z.-X. Shen, R. S. List, D. S. Dessau, F. Parmigiani, A. J. Arko, R. Bartlett, B. O. Wells, I. Lindau, and W. E. Spicer, Phys. Rev. B **42**, 8081 (1990).
- [77] K. Terakura, T. Oguchi, A. R. Williams, and J. Kübler, Phys. Rev. B **30**, 4734 (1984).
- [78] J. van Elp, R. H. Potze, H. Eskes, R. Berger, and G. A. Sawatzky, Phys. Rev. B **44**, 1530 (1991).
- [79] J. van Elp, H. Eskes, P. Kuiper, and G. A. Sawatzky, Phys. Rev. B **45**, 1612 (1992).
- [80] L. Messick, W. C. Walker, and R. Glosser, Phys. Rev. B **6**, 3941 (1972).
- [81] M. Takahashi and J. Igarashi, Phys. Rev. B **54**, 13566 (1996).
- [82] S. Massidda, A. Continenza, M. Posternak, and A. Baldereschi, Phys. Rev. B **55**, 13494 (1997).
- [83] O. Bengone, M. Alouani, P. Blochl, and J. Hugel, Phys. Rev. B **62**, 16392 (2000).
- [84] F. Aryasetiawan, Phys. Rev. B **46**, 13051 (1992).

